HHS Public Access

Author manuscript

Methods Enzymol. Author manuscript; available in PMC 2021 February 24.

Published in final edited form as:

Methods Enzymol. 2019 ; 615: 285–332. doi:10.1016/bs.mie.2018.08.017.

NMR Methods for Characterizing the Basic Side Chains of Proteins: Electrostatic Interactions, Hydrogen Bonds, and Conformational Dynamics

Dan Nguyen, **Chuanying Chen**, **B. Montgomery Pettitt**, **Junji Iwahara**[1]

Department of Biochemistry and Molecular Biology, Sealy Center for Structural Biology and Molecular Biophysics, University of Texas Medical Branch, Galveston, TX, United States

Abstract

NMR spectroscopy is a powerful tool for studying protein dynamics. Conventionally, NMR studies on protein dynamics have probed motions of protein backbone NH, side-chain aromatic, and CH_3 groups. Recently, there has been remarkable progress in NMR methodologies that can characterize motions of cationic groups in protein side chains. These NMR methods allow investigations of the dynamics of positively charged lysine (Lys) and arginine (Arg) side chains and their hydrogen bonds as well as their electrostatic interactions important for protein function. Here, describing various practical aspects, we provide an overview of the NMR methods for dynamics studies of Lys and Arg side chains. Some example data on protein–DNA complexes are shown. We will also explain how molecular dynamics (MD) simulations can facilitate the interpretation of the NMR data on these basic side chains. Studies combining NMR and MD have revealed the highly dynamic nature of short-range electrostatic interactions via ion pairs, especially those involving Lys side chains.

1. INTRODUCTION

To elucidate mechanisms underlying protein functions, it is essential to understand the atomic-level behavior of individual side chains at functionally important sites on proteins. Charged side chains and their electrostatic interactions are of fundamental importance for molecular recognition, association, and catalysis by proteins (Honig & Nicholls, 1995; Sheinerman, Norel, & Honig, 2000). The mobility of these side chains should affect electrostatic interactions and hydrogen bonds crucial for the functional activities of proteins. However, the dynamic aspects of these fundamental interactions involving the charged moieties of protein side chains are not well understood from experimentally obtained data.

Solution NMR spectroscopy is a powerful tool in experimental research on protein dynamics and has provided insight into dynamics–function relationship of proteins (Boehr, Dyson, & Wright, 2006; Clore & Iwahara, 2009; Loria, Berlow, & Watt, 2008; Mittermaier & Kay, 2009; Palmer, 2014). However, when protein dynamics are studied, the vast majority of NMR studies focus on the motions of either protein backbone or side-chain CH_3 groups.

[1]Corresponding author: j.iwahara@utmb.edu.

NMR investigations of polar or charged side chains remain rare. More investigations into the dynamic behavior of these side chains would deepen our knowledge about the functional roles of protein dynamics.

Our goal in this chapter is to provide other researchers with a practical overview of the NMR methods for dynamics investigations of lysine (Lys) and arginine (Arg) side chains. Hydrogen bonds and electrostatic interactions involving Lys side-chain NH_3^+ groups and Arg $N_\varepsilon H$ groups are of particular interest. Over the past decade, we have conducted NMR studies of basic side chains, primarily to obtain a better understanding of protein–DNA interactions. Lys and Arg side chains are crucial for electrostatic interactions with DNA phosphates and for recognition of DNA bases (Luscombe, Laskowski, & Thornton, 2001; Privalov, Dragan, & Crane-Robinson, 2011; Rohs et al., 2010). Due to our research background, the majority of the examples shown here are for protein–DNA complexes. However, the NMR methodology for Lys and Arg side chains introduced in this chapter is applicable to other protein systems as well. Furthermore, we explain how molecular dynamics (MD) simulations can facilitate interpretation of NMR data regarding the behavior of basic side chains.

2. NMR OF Lys AND Arg SIDE CHAINS

2.1 ^{1}H, ^{13}C, and ^{15}N Resonances of Lys/Arg Side Chains

2.1.1 Chemical Shifts and Protonation States—Typical ^{1}H, ^{13}C, and ^{15}N chemical shifts of Lys and Arg side chains of proteins are shown in Table 1. Side-chain methylene ^{1}H and ^{13}C resonances can be assigned using standard three-dimensional (3D) NMR spectra, such as HCCH-TOCSY, HCCH-COSY, H(CCO)NH, and C(CO)NH spectra (Clore & Gronenborn, 1998). ^{1}H and ^{15}N resonances from the $NH/NH_2/NH_3^+$ groups of Lys and Arg side chains are located in unique regions in ^{1}H–^{15}N heteronuclear spectra (e.g., see Fig. 1A), and additional experiments are required to assign these ^{1}H and ^{5}N resonances, as explained in Section 2.4. The NMR-based determination of the pK_a of protein side chains has been reviewed recently (Hass & Mulder, 2015; Platzer, Okon, & McIntosh, 2014). Because the typical pK_a of Lys side chains is 10.5, Lys side-chain amino groups are usually protonated in the form of NH_3^+ in neutral and acidic pH conditions. Lys side-chain $^{15}N_\zeta$ chemical shifts are typically 31–35 ppm in the protonated state (i.e., NH_3^+) (Andre, Linse, & Mulder, 2007; Iwahara et al., 2007; Poon et al., 2006). NH_3^+ groups that form a hydrogen bond with other moieties tend to exhibit a relatively large ^{15}N chemical shift (Blaum et al., 2010; Esadze, Li, Wang, Brüschweiler, & Iwahara, 2011; Sepuru, Iwahara, & Rajarathnam, 2018). The deprotonated state (i.e., NH_2) of a Lys side-chain amino group exhibits ^{15}N chemical shift of 22–26 ppm in the deprotonated state (Andre et al., 2007; Kougentakis et al., 2018; Poon et al., 2006; Takayama et al., 2008). The typical pK_a of Arg side chains has recently been updated to 13.8 (Fitch, Platzer, Okon, Garcia-Moreno, & McIntosh, 2015). Due to their typical pK_a values, the deprotonated states of Lys and Arg side chains are rare at physiological pH, especially for Arg. In this chapter, we focus on the positively charged, protonated states of Lys and Arg side chains.

2.1.2 Degenerate ^{1}H Resonances of Lys NH_3^+—

The resonances of the three ^{1}H nuclei within a Lys NH_3^+ group are degenerate due to rapid rotations around the C_ε–N_ζ bond. This degeneracy occurs even in the presence of hydrogen bonds with other moieties. For example, in ubiquitin, the Lys27 NH_3^+ group forms three hydrogen bonds with other moieties, but the bond rotations of this NH_3^+ occur on a nanosecond timescale, making the ^{1}H resonances of its three ^{1}H nuclei completely degenerate (Esadze et al., 2011). As described in Section 5, the hydrogen bonding of Lys side chains is dynamic, allowing rapid C_ε–H_ζ bond rotations. The intrinsic ^{15}N transverse relaxation of Lys NH_3^+ is very slow owing to the rapid C_ε–N_ζ bond rotations. Although rapid hydrogen exchange with water causes some adverse effects on NMR experiments (see Section 2.3), heteronuclear ^{1}H–^{15}N NMR of Lys NH_3^+ groups is useful for investigating the conformational dynamics, hydrogen-bond dynamics, and ion-pair dynamics of proteins.

2.1.3 Hindered 180° Rotations of Arg Guanidinium C_ζ–N Bonds—

Arg side-chain guanidinium moieties involve five hydrogen (H_ε, $H_{\eta 11}$, $H_{\eta 12}$, $H_{\eta 21}$, and $H_{\eta 22}$) and three nitrogen (N_ε, $N_{\eta 1}$, and $N_{\eta 2}$) atoms. In general, it is relatively easy to analyze the ^{1}H and ^{15}N resonances of $N_\varepsilon H$ groups but not those of $N_\eta H_2$ groups. The so-called hindered 180° rotations along the N_ε–C_ζ, C_ζ–$N_{\eta 1}$, and C_ζ–$N_{\eta 2}$ bonds within each planar guanidinium moiety cause interconversions between the two $N_\eta H_2$ groups and between the two hydrogen atoms of each $N_\eta H_2$ group. These interconversions tend to occur in the intermediate exchange regime on the ^{1}H and ^{15}N chemical shift timescale at physiological temperature (Yamazaki et al., 1995). Because these interconversions cause severe broadening of $^1H_\eta$ resonances, the four $^1H_\eta$ resonances of Arg $N_\eta H_2$ groups are rarely isolated. This broadening effect makes the NMR investigations of Arg $N_\eta H_2$ groups challenging, though quantitative kinetic analysis of the C_ζ–N bond rotationsis possible in favorable cases (Gerecht, Figueiredo, & Hansen, 2017; Nieto et al., 1997). In contrast, the ^{1}H and ^{15}N resonances of Arg $N_\varepsilon H$ groups are unaffected by the hindered 180° bond rotations and exhibit relatively sharp NMR signals when the hydrogen exchange is slow enough. Thus, $N_\varepsilon H$ groups are most convenient for ^{1}H–^{15}N NMR investigations of Arg side-chain guanidinium moieties.

2.2 Impact of Hydrogen Exchange on Lys/Arg Side-Chain NMR

2.2.1 Direct Influence of Hydrogen Exchange on ^{1}H Line Shapes—

Hydrogen exchange with water broadens the ^{1}H line shapes of signals from the $NH/NH_2/NH_3^+$ groups of Arg and Lys side chains. When direct ^{1}H observation of a particular NH, NH_2, or NH_3^+ group is possible, its hydrogen exchange rate, $k_{ex,w}$, is typically <200 s^{-1}. This corresponds to a slow exchange regime on the NMR chemical shift timescale because the ^{1}H chemical shift difference ($\Delta\delta$) between $NH/NH_2/NH_3^+$ and water resonances is typically >1000 Hz (i.e., $k_{ex,w} \ll 2\pi\Delta\delta$). This slow exchange increases the apparent ^{1}H transverse relaxation rate by the first-order rate constant for the transition from $NH/NH_2/NH_3^+$ to water. Note that this rate constant is virtually identical to the hydrogen exchange rate $k_{ex,w}$ (sum of the rate constants for the forward and backward transitions), since the population of water is far larger in this exchange. Therefore, the line width of the ^{1}H signal from $NH/NH_2/NH_3^+$ is broadened by $k_{ex,w}/\pi$Hz due to hydrogen exchange.

2.2.2 Indirect Influence of Hydrogen Exchange on ^{15}N Line Shapes—

Hydrogen exchange impacts the ^{15}N dimension unless in-phase single-quantum coherence is maintained throughout the ^{15}N evolution period. This broadening effect on the ^{15}N dimension is easier to understand for HMQC because multiple-quantum terms such as $2N_xH_y$ should be impacted by hydrogen exchange in the manner explained above. Actually, hydrogen exchange broadens ^{15}N line shapes not only in HMQC spectra but also in HSQC spectra. The impact of hydrogen exchange on ^{15}N line shape in HSQC spectra occurs through scalar relaxation of antiphase single-quantum terms (Iwahara et al., 2007). In the first half of the ^{15}N evolution period ($t_1/2$) before a ^{1}H 180° pulse, the $2N_yH_z$ term generated through the first INEPT scheme produces $2N_xH_z$, N_x, and N_y terms for NH; $2N_xH_z$, N_x, N_y, $4N_xH_zH_z$, and $4N_yH_zH_z$ for NH_2; and $2N_xH_z$, N_x, N_y, $4N_xH_zH_z$, $4N_yH_zH_z$, $8N_xH_zH_zH_z$, and $8N_yH_zH_zH_z$ for NH_3^+ groups. For antiphase single-quantum ^{15}N transverse terms with respect to ^{1}H, scalar relaxation arises from autorelaxation of the coupled ^{1}H nuclei (Abragam, 1961; Bax, Ikura, Kay, Torchia, & Tschudin, 1990) and substantially increases the relaxation rates of the $2N_{x(y)}H_z$, $4N_{x(y)}H_zH_z$, and $8N_{x(y)}H_zH_zH_z$ terms, compared to the relaxation rates of the in-phase single-quantum terms $N_{x(y)}$. The scalar relaxation rate R_{sc} for each ^{1}H nucleus is given by $R_{sc} = \rho_{HH} + k_{ex,w}$, where ρ_{HH} is the rate of autorelaxation arising from dipole–dipole (DD) interactions with external ^{1}H nuclei (Iwahara et al., 2007). Scalar relaxation rates for the N_+, $2N_+H_z$, $4N_{+H_zH_z}$, and $8_{N+}H_zH_zH_z$ terms are 0, R_{sc}, $2R_{sc}$, and $3R_{sc}$, respectively (Esadze et al., 2011). The hydrogen exchange rate $k_{ex,w}$ is typically faster than ρ_{HH} rates and intrinsic ^{15}N relaxation rates, and therefore governs ^{15}N line shapes in HSQC spectra for NH_3^+ groups (Anderson et al., 2013; Esadze et al., 2011; Iwahara et al., 2007; Zandarashvili, Esadze, & Iwahara, 2013). In HSQC, hydrogen exchange broadens ^{15}N line width by $1.5k_{ex,w}/\pi$ Hz for Lys NH_3^+ groups and by $0.5k_{ex,w}/\pi$Hz for Arg $N_\varepsilon H$ groups. The impacts of scalar relaxation and hydrogen exchange on the ^{15}N dimension of heteronuclear ^{1}H–^{15}N correlation experiments are summarized in Fig. 2A and B.

2.2.3 Self-decoupling Due to Hydrogen Exchange—

Due to the self-decoupling effect (Cavanagh, Fairbrother, Palmer, Rance, & Skelton, 2007; Harbison, 1993), the apparent magnitude of J-coupling between the ^{15}N and ^{1}H nuclei of $NH/NH_2/NH_3^+$ becomes smaller than the intrinsic value when the hydrogen exchange rate is comparable to or faster than $\pi^1 J_{NH}\,s^{-1}$. Theoretical consideration of the self-decoupling effect through hydrogen exchange is presented in the supporting information of Takayama et al. (2008). Because the hydrogen exchange rates for Lys NH_3^+ groups at pH > 7 are typically far greater than $\pi^1 J_{NH}$ (Segawa, Kateb, Duma, Bodenhausen, & Pelupessy, 2008), self-decoupling of $^1J_{NH}$ can easily occur for Lys side chains. Under such conditions, H2(C)N spectra recorded without ^{1}H decoupling in the ^{15}N dimension exhibit singlet (rather than quartet) ^{15}N resonances of Lys NH_3^+ groups due to the self-decoupling effect.

2.3 Importance of Maintaining In-Phase Single-Quantum ^{15}N Coherence

2.3.1 HISQC Drastically Improves Lys NH_3^+ ^{15}N Line Shapes—

To avoid the severe broadening of ^{15}N line shapes due to rapid scalar relaxation arising from hydrogen exchange, Iwahara et al. developed NH_3^+-selective heteronuclear in-phase single-quantum coherence (HISQC) and its derivatives (Iwahara et al., 2007). The pulse sequence of the

HISQC experiment is shown in Fig. 2C. In this $^{1}H–^{15}N$ heteronuclear correlation experiment, the in-phase single-quantum term N_x or N_y is created at the beginning of the ^{15}N evolution period, and the in-phase single-quantum coherence N_+ ($=N_x + iN_y$) is maintained via the ^{1}H WALTZ decoupling scheme throughout the evolution period. By maintaining the in-phase single-quantum terms N_x and N_y and thereby removing the scalar relaxation from the t_1 time domain for the ^{15}N dimension, the HISQC experiment drastically improved the sensitivity and resolution in detection of signals from NH_3^+ groups, compared to the corresponding HMQC and HSQC experiments (Fig. 2D). Although the typical range of the ^{15}N chemical shifts of Lys NH_3^+ groups is relatively narrow, the signal dispersion in HISQC spectra is typically excellent owing to the intrinsically slow ^{15}N transverse relaxation of NH_3^+ groups. Many NMR pulse sequences for NH_3^+ groups have implemented the principle of HISQC and minimized the adverse impacts of scalar relaxation of antiphase terms with respect to ^{1}H nuclei (Anderson et al., 2013; Esadze et al., 2011; Esadze, Zandarashvili, & Iwahara, 2014; Iwahara et al., 2007; Zandarashvili et al., 2013; Zandarashvili, Li, Wang, Brüschweiler, & Iwahara, 2011).

2.3.2 HISQC Can Also Improve Arg $^{15}N_\varepsilon$ Line Shapes—

The hydrogen exchange rates $k_{ex,w}$ of Arg $N_\varepsilon H$ groups are generally slower than those of Lys NH_3^+ group. Furthermore, while hydrogen exchange of Lys NH_3^+ groups broadens the Lys ^{15}N line width by $1.5k_{ex,w}/\pi$ in HSQC, hydrogen exchange of Arg $N_\varepsilon H$ groups broadens the Arg ^{15}N line width only by $0.5k_{ex,w}/\pi$ (see Fig. 2B). Because of the smaller impact of scalar relaxation arising from hydrogen exchange, the advantage of $^{1}H–^{15}N$ HISQC for Arg $N_\varepsilon H$ groups is not as great as that for Lys NH_3^+groups. However, when hydrogen exchange is rapid (e.g., due to a relatively high pH), the HISQC spectra of Arg $N_\varepsilon H$ groups can be significantly better than the HSQC spectra (Yuwen & Skrynnikov, 2014a). To maximize the sensitivity for Arg $N_\varepsilon H$ groups, the delay ω_b in the HISQC pulse sequence in Fig. 2D should be set to 2.7 ms. This setting also suppresses signals from Arg $N_\eta H_2$ groups and simplifies the spectrum, allowing the use of a narrower spectral width for the ^{15}N dimension. TROSY for Arg $N_\varepsilon H$ groups is not as advantageous as that for backbone NH groups because the ^{15}N chemical shift anisotropy (CSA) of Arg N_ε (−114 ppm) (Trbovic et al., 2009) is significantly smaller than that of backbone N (−162 to −173 ppm) (Yao, Grishaev, Cornilescu, & Bax, 2010). The ^{15}N dimension of TROSY also suffers from scalar relaxation arising from hydrogen exchange.

2.4 Resonance Assignment for Lys/Arg Side Chains

2.4.1 Resonance Assignment for Lys Side-Chain NH_3^+ Groups—

Several ^{1}H, ^{3}C, ^{5}N triple-resonance experiments for resonance assignment of Lys side-chain amino groups have been developed (Andre et al., 2007; Esadze et al., 2014; Iwahara et al., 2007). Resonance assignment for Lys side-chain NH_3^+ groups requires long-range correlation spectra. Short-range correlations between NH_3^+ and $^{1}H_\varepsilon/^{13}C_\varepsilon$ resonances are usually insufficient for unambiguous assignment due to poor dispersion of their chemical shifts. Due to high mobility, few $^{1}H–^{1}H$ NOE cross-peaks are observed for Lys NH_3^+ groups, rendering NOE-based resonance assignment difficult. We found that the combined use of (H2C)N(CC)H-TOCSY, H3NCECD, H3NCG, H2(C)N, and HISQC spectra can greatly facilitate assignment of ^{1}H and ^{15}N resonances for Lys side-chain NH_3^+ groups (Esadze et al., 2014).

Fig. 3 shows an example of this approach. H2(C)N (Andre et al., 2007) and (H2C)N(CC)H-TOCSY (Esadze et al., 2014) experiments allow observation of the ^{15}N resonances of Lys NH_3^+ groups even if direct ^1H detection of the NH_3^+ groups is impossible due to their rapid hydrogen exchange. Because multiple side-chain ^1H resonances are observed at high resolution along the ^1H direct-detection dimension with excellent separation by sharp $^{15}N_\zeta$ resonances, the (H2C)N(CC)H-TOCSY spectrum greatly facilitates $^{15}N_\zeta$ resonance assignment for Lys NH_3^+ groups. The temperature dependence of the H2(C)N spectra allows us to track the change in $^{15}N_\zeta$ resonances as a function of temperature. These data together with the 3D H3NCG and H3NCECD spectra allowed us to unambiguously assign ^1H–^{15}N HISQC signals from the Lys NH_3^+ groups of some protein–DNA complexes at relatively low temperature.

2.4.2 Resonance Assignment for Arg Guanidinium Moieties—Some ^1H, ^3C, ^5N triple-resonance experiments on Arg side chains have been proposed (Andre et al., 2007; Iwahara & Clore, 2006; Yamazaki et al., 1995). Compared to the guanidinium $N_\eta H_2$ moieties, Arg $^{15}N_\varepsilon$ and $^1H_\varepsilon$ resonances are relatively easy to assign. When broadband ^{15}N 180° pulses are used, 3D HNCACB for backbone amide groups also gives signals from Arg side chains, which correlate Arg side-chain $^1H_\varepsilon$, $^{15}N_\varepsilon$, and $^{13}C_\gamma/^{13}C_\delta$ resonances (Iwahara & Clore, 2006). Alternatively, the same correlation signals can be observed selectively for Arg side chains by using $^{15}N_\varepsilon$-selective pulses (see Section 2.4.3) in 3D HNCACB. NOE cross-peaks of $^1H_\varepsilon$ nuclei in 3D ^{15}N-edited NOESY also facilitate resonance assignment for Arg $N_\varepsilon H$ groups. Fig. 4 shows an example of Arg $^{15}N_\varepsilon$ and $^1H_\varepsilon$ resonance assignment based on $^{13}C_\gamma/^{13}C_\delta$ resonances and NOE data. Some double- or triple-resonance experiments were developed for resonance assignment of Arg side-chain $N_\eta H_2$ groups (Gerecht et al., 2017; Löhr & Rüterjans, 1998; Yamazaki et al., 1995), though this is more challenging due to the above-mentioned hindered 180° rotations that tend to occur in the intermediate exchange regime at physiological temperature.

2.4.3 Selective ^{15}N Pulses for Lys and Arg Side Chains—The ^{15}N resonances of Lys (~25–35 ppm) and Arg (~65–90 ppm) side chains are significantly different from those of protein backbone (~105–135 ppm). Largely because the practically available RF strength for the ^{15}N channel is relatively weak (up to ~7 kHz), standard ^1H–^{15}N NMR experiments optimized for the backbone give significantly compromised signals from Lys and Arg side chains (Iwahara & Clore, 2006; Iwahara et al., 2007). The pulse imperfection for off-resonance ^{15}N nuclei adversely impacts quantitative ^1H–^{15}N heteronuclear NMR experiments, particularly measurements of ^{15}N transverse relaxation rates. The simultaneous observation with a reasonably high digital resolution for ^{15}N requires aliasing in the ^{15}N dimension, which can cause accidental overlaps of nonaliased and aliased signals. For these reasons, we typically conduct ^1H–^{15}N NMR experiments for the backbone, Arg side chains, and Lys NH_3^+ groups separately. For selective observation of Lys or Arg side-chain signals, we use 1-ms rSNOB pulses (Kupče et al., 1995) as ^{15}N 180° pulses selective for Lys NH_3^+ or Arg $N_\varepsilon H$ ^{15}N nuclei. The rSNOB pulse works as an inversion pulse for N_z and as a refocusing pulse for N_x and N_y magnetizations. The bandwidth of a 1-ms rSNOB pulse is approximately ±1.1 kHz and is well suited to selectively observe either Arg $^{15}N_\varepsilon$ (75–90

ppm) nuclei or Lys $^{15}N_{\zeta}$ (30–35 ppm; NH_3^+) nuclei. We incorporate ^{15}N rSNOB pulses into many Lys- or Arg-selective NMR experiments.

2.4.4 Chemical Approach—A chemical approach can be used for resonance assignment of basic side chains that form intermolecular ion pairs with DNA or RNA (Anderson et al., 2015). In this approach, ^1H–^{15}N correlation spectra for the basic side chains of the protein–DNA (or RNA) complexes are compared with and without oxygen-to-sulfur substitution in a backbone phosphate group. This chemical modification is relatively mild because it retains the tetrahedral geometry and overall charge of the phosphate group. Thiophosphoramidites, which are commercially available from Glen Research Co., allow synthesis of DNA containing phosphorodithioate using standard DNA synthesizers. Site-specific oxygen-to-sulfur substitution in a backbone phosphate significantly perturbs the NMR chemical shifts of the interfacial cationic group at the modification site and allows one to identify the NMR signal from the interfacial Lys or Arg groups. This approach was demonstrated initially with dithioate derivatives of phosphate (Anderson et al., 2015) and later with monothioate derivatives of phosphate (Nguyen, Zandarashvili, White, & Iwahara, 2016). Although synthesis of DNA/RNA containing a monothioate derivative produces a mixture of R_P and S_P diastereomers, chromatographic separation of these two forms is possible (Frederiksen & Piccirilli, 2009; Nguyen et al., 2016).

2.5 Sample Conditions for NMR Studies of Lys/Arg Cations

2.5.1 Two Critical Factors: pH and Temperature—A major challenge for NMR studies of Lys NH_3^+ and Arg $N_{\varepsilon}H$ groups is their rapid hydrogen exchange with water. For example, the hydrogen exchange rates for Lys NH_3^+ groups can exceed $1000s^{-1}$ at pH 7.5 and 27°C (Segawa et al., 2008). Under such conditions, direct observation of the ^1H signals from Lys NH_3^+ groups is virtually impossible. However, direct ^1H detection can become possible if hydrogen exchange is substantially slowed down due to (1) lower pH, (2) lower temperature, or (3) structural effects such as hydrogen bonding and steric hindrance (Esadze et al., 2011; Iwahara et al., 2007; Poon et al., 2006; Takayama et al., 2008; Tomlinson, Ullah, Hansen, & Williamson, 2009). For the feasibility of heteronuclear ^1H–^{15}N NMR experiments for Lys and Arg side chains, temperature and pH are two critical factors that should be set carefully.

The dependence of hydrogen exchange rates on pH is particularly strong. In general, a decrease in pH by 1 unit reduces the hydrogen exchange rate by a factor of 10 (Englander, Downer, & Teitelbaum, 1972; Liepinsh & Otting, 1996). For example, if the pH is decreased from 7.5 to 5.8, the hydrogen exchange rates become 50-fold slower. It should be noted that hydrogen exchange rates depend on the buffer used (e.g., slower in a succinate buffer than in a phosphate buffer at the same pH). The temperature dependence of hydrogen exchange rates is also strong. Upon a decrease in temperature by 10°C, hydrogen exchange rates become ~two- to fourfold slower for Lys NH_3^+ and Arg $N_{\varepsilon}H$ groups, depending on the activation energy. The temperature dependence of hydrogen exchange seems to be stronger for Arg $N_{\varepsilon}H$ groups than for Lys NH_3^+ groups (Segawa et al., 2008). We typically conduct NMR experiments on Lys and Arg side chains at pH 5–6 and 2–35°C.

2.5.2 Coaxial NMR Tubes to Avoid Partial Deuteration by D_2O—For quantitative NMR experiments on Lys NH_3^+ and Arg $N_\varepsilon H$ groups, a D_2O for NMR lock should not be included in the sample buffer. In general, the ^{15}N chemical shifts of $NH/NH_2/NH_3^+$ moieties are significantly different when they are partially deuterated in the form of NHD, NH_2D, or NHD_2 by D_2O. The partial deuteration causes not only additional signals (see Fig. 1B) (Iwahara et al., 2007) but also additional broadening effects on the ^{15}N dimension due to the exchange between ^1H-attached and ^2H-attached states for which ^{15}N resonances differ (Yuwen & Skrynnikov, 2014a). We use coaxial NMR tubes to resolve the problems arising from deuterated $NH/NH_2/NH_3^+$ moieties by separating D_2O from the sample solution. The sample solution (typically, 0.4–1.0 m*M* protein) does not contain D_2O, and therefore, deuteration of $NH/NH_2/NH_3^+$ moieties does not occur. Depending on the applications, we use two different configurations of NMR coaxial tubes (Fig. 1C). In one type of NMR coaxial tube (e.g., Shigemi cat. # SC-002), the protein solution is in the inner tube, and D_2O is in the outer tube. For this type, we use a sample solution in the inner tube (270 μL) and D_2O in the outer tube (~100 μL). In the other type of NMR coaxial tube (e.g., Norell cat. # NI5CCI-B), we use a sample solution in the outer tube (370 μL) and D_2O in the inner stem (~ 100 μL). In general, this type of configuration with a thin inner stem gives a higher sensitivity for the same solution, mainly because the sample molarity in the detected region of the tube is higher due to a larger volume. However, a practical problem about this coaxial tube is that shimming is more difficult. Shimming for coaxial tube samples should not rely on deuterium signals because D_2O and the sample solution are located in different compartments. In our experience, the gradient shimming method based on H_2O imaging (van Zijl, Sukumar, Johnson, Webb, & Hurd, 1994) works fine in the one-dimensional mode but not in the three-dimensional mode to achieve magnetic-field homogeneity of solution samples in coaxial NMR tubes. When a high-salt concentration is required, the configuration with the sample in the inner tube is more suitable for the reason described in some papers on NMR studies of high ionic-strength samples (Takeda et al., 2011; Voehler, Collier, Young, Stone, & Germann, 2006).

2.5.3 Dealkalization of NMR Tubes—Due to the intrinsically rapid hydrogen exchange, the ^1H signals from Lys side-chain NH_3^+ groups are sensitive to an increase in pH. Previously, we often found that a gradual increase in pH occurred over a few weeks in NMR tubes even in the presence of buffer. This increase was noticeable in NMR experiments because the signals from Lys NH_3^+ groups became significantly weaker or even disappeared due to the more rapid hydrogen exchange. In fact, the original spectra of such samples were restored through buffer exchange. We speculate that the increase in pH might be due to gradual contamination of sodium ions leached from the glass surface through the Na^+–H^+ exchange mechanism (Bunker, 1994). We found that dealkalization treatment of NMR tubes can prevent the gradual increase in pH. In this treatment, we put 0.5 *M* nitric acid into coaxial NMR tubes, incubate the tubes in a hot water bath (60–80°C) for 2–3 h, extensively wash the tubes with pure water, and dry them in a heat dryer. We routinely perform this dealkalization for new coaxial tubes before their use for NMR experiments on Lys NH_3^+ and Arg $N_\varepsilon H$ groups.

3. CONFORMATIONAL DYNAMICS OF Lys/Arg SIDE CHAINS

The ^{15}N NMR relaxation and scalar coupling data of Lys NH_3^+ and Arg $N_\varepsilon H$ groups can provide information on the mobility of the cationic moieties of these basic side chains. Here, we describe practical aspects of the analysis of the conformational dynamics of Lys and Arg side chains.

3.1 ^{15}N Relaxation Analysis for Lys NH_3^+ Groups

The theoretical details of the ^{15}N relaxation of Lys side-chain NH_3^+ groups are somewhat complicated due to cross-correlation within the AX_3 spin system and are beyond the scope of this chapter. Readers interested in the theoretical issues regarding the ^{15}N relaxation of Lys NH_3^+ groups should refer to our previous publication (Esadze et al., 2011). General descriptions of the cross-correlation effects on the NMR relaxation of AX_3 spin systems can be found in other articles (Kay & Torchia, 1991; Kumar, Grace, & Madhu, 2000; Ollerenshaw, Tugarinov, & Kay, 2003).

3.1.1 Removal of Adverse Effects of Multispin Terms—Fig. 5 shows the pulse sequences used to measure ^{15}N relaxation for Lys side-chain NH_3^+ groups. The first step for measuring ^{15}N longitudinal (R_1) and transverse (R_2) relaxation rates is to create the ^{15}N in-phase single-quantum term via coherence transfer from ^{1}H to ^{15}N nuclei through a refocused INEPT scheme (Ernst, Bodenhausen, & Wokaun, 1987). The product operator terms N_x, $2N_yH_z$, $4N_xH_zH_z$, and $8N_yH_zH_zH_z$ are generated in the period of $2\tau_b$ in the first refocused INEPT scheme of our pulse sequence for ^{15}N R_1 and R_2 measurements. The $2N_yH_z$ and $8N_yH_zH_zH_z$ terms are eliminated by the pulsed field gradient (PFG) g_4 after the ^{1}H 90°($-x$) and ^{15}N 90°(γ) pulses at the end of the refocused INEPT scheme, but the $4N_xH_zH_z$ term is not eliminated because a PFG alone cannot destroy the homonuclear zero-quantum coherence $4N_zH_yH_y$ (van de Ven, 1995). The coefficients of the transfers from $2N_yH_z$ to N_x and to $4N_xH_zH_z$ are given by $\cos^2\theta\sin\theta$ and $(3\cos^2\theta - 1)\sin\theta$, respectively, in which $\theta = 2\pi\ ^1J_{NH}\ \tau_b$ and $^1J_{NH}$ represents the one-bond ^{1}H–^{15}N scalar coupling constant (Ernst et al., 1987). The use of the time τ_b satisfying $3\cos^2\theta - 1 = 0$ thus eliminates the $4N_xH_zH_z$ term but retains the N_x term, and this condition is achieved by $\rho_b = 2.1$ ms in the original pulse sequences (Esadze et al., 2011). This approach was also used for ^{13}C R_1 and R_2 relaxation measurements for protein CH_3 groups (Kay et al., 1992; Palmer, Wright, & Rance, 1991). A practical problem of this approach is that it reduces the efficiency of the transfer from $2N_yH_z$ to N_x (i.e., $\cos^2\theta\sin\theta$) and weakens the signals from NH_3^+ groups. Recently, we resolved this problem by implementing schemes that eliminate any contributions arising from $4N_xH_zH_z$ (Nguyen, Lokesh, et al., 2017). The pulse sequences shown in Fig. 5 implement such schemes and allow the use of $\tau_b = 1.3$ ms to maximize $\cos^2\theta\sin\theta$, improving the sensitivity by a factor of 1.8 without compromising the accuracy in ^{15}N relaxation measurements (Nguyen, Lokesh, et al., 2017).

3.1.2 ^{15}N R_1 Relaxation Measurements for Lys NH_3^+ Groups—The ^{15}N R_1 relaxation rates of Lys side-chain NH_3^+ groups are typically 0.2–1.5 s^{-1} at the ^{1}H frequencies of 600–800 MHz. To measure the Lys ^{15}N R_1 rates with the pulse sequence shown in Fig. 5A, we typically record eight spectra in an interleaved manner with different

lengths for the relaxation period T_r (=0.1, 0.2, 0.4, 0.6, 0.9, 1.2, 1.6, and 2.1 s). The minimum delay, T_r = 0.1 s, is long enough to let the $4N_zH_yH_y$ term completely decay through its rapid relaxation (Nguyen, Lokesh, et al., 2017). We record the eight datasets in an interleaved manner, typically with 16 scans per free induction decay (FID) using a cryogenic probe. The total time for recording is ~20–30 h. The ^{15}N R_1 rates are determined through nonlinear least-squares fitting with a single exponential function.

3.1.3 ^{15}N R_2 Relaxation Measurements for Lys NH_3^+ Groups—Owing to rapid C_ε–N_ζ bond rotations, the Lys side-chain NH_3^+ groups exhibit very slow ^{15}N transverse relaxation. For the protein–DNA complexes we studied (17–30 kDa), while ^{15}N T_2 relaxation times for the protein backbone NH groups were 50–80 ms, those for the Lys NH_3^+ groups were typically >300 ms even for the Lys side chains that form ion pairs with DNA. Fig. 5B shows the pulse sequence for the ^{15}N transverse relaxation measurement, in which the CW-CPMG scheme (Hansen et al., 2008) is implemented to maintain the in-phase single-quantum coherence N_+. This scheme contains two CPMG blocks (Carr & Purcell, 1954; Meiboom & Gill, 1958) that sandwich a refocusing pulse, and the ^{1}H continuous wave (CW) is applied to eliminate scalar relaxation during each CPMG blocks. As is known for ^{13}C transverse relaxation for CH_3 groups, the ^{15}N transverse relaxation for NH_3^+ groups should intrinsically be biexponential due to the strong effects of DD–DD cross-correlation between three ^{15}N–^{1}H DD interactions (Esadze et al., 2011). However, the biexponential decay and single-exponential decay according to $\exp(-R_{2,ini}T)$ are virtually indistinguishable for the first 30% of decay, for which the use of single-exponential fitting for determination of the initial transverse relaxation rate $R_{2,ini}$ is valid (Esadze et al., 2011). The theoretical expression of the $R_{2,ini}$ rate is formulated in Esadze et al. (2011), and its practical use is described below (Section 3.3). Due to the use of only <30% decay, measurements of $R_{2,ini}$ rates for Lys NH_3^+ groups are typically not as precise as those of R_1 rates in terms of error percentage. To compensate for this problem, we measure the ^{15}N $R_{2,ini}$ rates using a larger number of scans (32 scans per FID) than that for ^{15}N R_1 measurements. We typically record nine spectra in an interleaved manner with different lengths for the transverse relaxation period (up to 120 ms). The total time for recording ^{15}N transverse relaxation data for Lys NH_3^+ groups is ~35–50 h.

The pulse sequence shown in Fig. 5B can also be used to detect microsecond to millisecond timescale motions of NH_3^+ groups (Esadze et al., 2011) because the CW-CPMG scheme is well suited for relaxation dispersion experiments (Baldwin, Hansen, Vallurupalli, & Kay, 2009; Hansen et al., 2008). In fact, the relaxation dispersion data recorded with various CPMG frequencies in this pulse sequence were used to study the slow dynamics of Lys NH_3^+ groups (Esadze et al., 2016, 2011).

3.1.4 Heteronuclear ^{15}N NOE for Lys NH_3^+ Groups—Due to rapid C_ε–N_ζ bond rotations, heteronuclear NOEs for Lys side-chain NH_3^+ groups are negative and typically ranges from −1.8 to −3.3. The pulse sequence to record heteronuclear ^{15}N NOE data for Lys NH_3^+ groups is shown in Fig. 5C (Esadze et al., 2011; Nguyen, Lokesh, et al., 2017). The effects of DD/DD cross-correlation, which causes transitions between N_z and $4N_zH_zH_z$ terms and between H_z and $4N_zH_zH_z$ terms, are simplified by using 180° pulses instead of

120° pulses in the ^{1}H saturation period (Esadze et al., 2011). Incomplete recovery of water ^{1}H magnetization can introduce substantial errors in the heteronuclear NOEs and this problem is particularly serious when hydrogen exchange is rapid (Grzesiek & Bax, 1993; Idiyatullin, Daragan, & Mayo, 2001; Li & Montelione, 1994; Skelton et al., 1993). In the pulse sequence shown in Fig. 5C, this problem is avoided by implementation of the water-flip-back scheme (Grzesiek & Bax, 1993) and the use of a very long recycle delay (Renner, Schleicher, Moroder, & Holak, 2002). Our recycle delays in the heteronuclear NOE experiments for Lys NH_3^+ groups are 12 and 18 s at the ^{1}H frequencies of 600 and 800 MHz, respectively. If a shorter time is used, the magnitude of heteronuclear NOE may appear to be larger due to weaker signal intensity in the reference spectrum. With 48 scans per FID and 100 complex points for each subspectrum, the total recording time is typically ~55–80h.

3.2 ^{15}N Relaxation Analysis for Arg $N_\varepsilon H$ Groups

3.2.1 NMR Relaxation Measurements for Arg $^{15}N_\varepsilon$ Nuclei—

The pulse sequences shown in Fig. 5 can be used to measure ^{15}N R_1, R_2, and heteronuclear NOE for Arg side-chain $N_\varepsilon H_\varepsilon$ groups as well, though changes in some parameters are required due to the differences between Lys NH_3^+ and Arg $N_\varepsilon H$ groups. The caption of Fig. 5 shows the required changes, many of which are related to the different spin systems (AX_3 vs AX) and $^{1}J_{NH}$ coupling constants (74 vs 92 Hz) of Lys NH_3^+ and Arg $N_\varepsilon H$ groups. In the ^{15}N relaxation measurements for Arg $N_\varepsilon H$ groups, we typically use a ^{15}N carrier position at ~84ppm and a ^{15}N spectral width of ~6–12ppm. These settings together with the use of ^{15}N rSNOB 180° pulses in the INEPT schemes allow ^{15}N relaxation measurements for Arg side-chain $^{15}N_\varepsilon$ nuclei only. Although simultaneous detection of Arg side-chain $^{15}N_\varepsilon$ and backbone ^{15}N nuclei is possible, separate measurements have the following advantages. First, selective observation of Arg $^{15}N_\varepsilon$ allows the use of a narrower ^{15}N spectral width for a high resolution without any concerns about undesired overlaps with folded signals from backbone NH or Lys NH_3^+ groups. Second, R_2 measurements with the ^{15}N carrier position set to the Arg N_ε resonance allow application of on-resonance 180° pulses in the CPMG scheme. Simultaneous R_2 measurements of backbone and Arg side-chain ^{15}N nuclei require the use of a ^{15}N carrier position that introduces significant off-resonance effects to the CPMG scheme (Korzhnev, Tischenko, & Arseniev, 2000) and decrease the data quality for either type of ^{15}N nuclei. Furthermore, selective observation of Arg $N_\varepsilon H$ groups allows higher sensitivity because the conditions optimized for backbone NH groups considerably weaken the signals from Arg $N_\varepsilon H$ groups unless broadband ^{15}N 180° pulses are used (Iwahara & Clore, 2006). For these reasons, we conduct the ^{15}N relaxation experiments for backbone NH groups, Lys NH_3^+ groups, and Arg $N_\varepsilon H$ group separately.

3.2.2 Impact of ^{15}N–^{15}N Couplings on Arg $^{15}N_\varepsilon$ R_2 Measurements—

The presence of two geminal couplings to $^{15}N_{\eta 1}$ and $^{15}N_{\eta 2}$ nuclei can in principle affect measurements of transverse relaxation of Arg $^{15}N_\varepsilon$ nuclei. However, our recent study shows that the impact of the $^{2}J_{NN}$ couplings on CPMG-based transverse relaxation measurements for Arg $^{15}N_\varepsilon$ nuclei is typically negligible (Nguyen & Iwahara, 2018). This result is due to the relatively small magnitudes of the $^{2}J_{NN}$ couplings (1.1–1.3 Hz) and also due to the so-called SITCOM mechanism (Dittmer & Bodenhausen, 2006) that efficiently quenches

homonuclear J modulation. The use of selective refocusing pulses (e.g., REBURP) in the CPMG scheme was previously proposed to avoid modulation through the homonuclear ^{15}N–^{15}N scalar couplings (Yuwen & Skrynnikov, 2014b). However, the use of long shaped pulses during the CPMG scheme allows only low ν_{CPMG} frequencies, which may not completely cancel the exchange contribution to the measured R_2 relaxation rates. Such use of $^{15}N_\varepsilon$-selective shaped pulses during the CPMG scheme is unnecessary because the SITCOM effect effectively quenches the evolution of $^2J_{NN}$ couplings of Arg side chains during the CPMG scheme with typical rectangular ^{15}N 180° pulses. However, the $^{15}N_\varepsilon$ R_2 rates may be overestimated for very mobile Arg side chains, if the following condition (*recoupling condition*) (Aeby & Bodenhausen, 2008) is accidentally met:

$$\Omega_S/(2\pi) = 4n\nu_1\nu_{CPMG}/(2\nu_1 + \nu_{CPMG}) \quad (1)$$

where n is an integer; $\Omega_S/(2\pi)$, the offset in Hz for off-resonance spin S; ν_1, the RF strength in Hz for refocusing pulses; ν_{CPMG}, the CPMG field frequency in Hz. When $\nu_1 \gg \nu_{CPMG}$, Eq. (1) becomes $\Omega_S/(2\pi) \approx 2n\nu_{CPMG}$. When the difference between $\Omega_S/(2\pi)$ and the nearest recoupling condition is less than 10% of ν_{CPMG}, significant amplitude modulation occurs and the apparent R_2 rate becomes larger than the actual R_2 relaxation rate. Not surprisingly, this adverse effect is weaker for a smaller magnitude of the homonuclear J coupling. When $\Omega_S/(2\pi)$ is more significantly different from the recoupling conditions, effectively complete quenching of J-modulation occurs, allowing accurate measurements of the R_2 rates. Recoupling conditions can be readily avoided through appropriate settings of the CPMG frequency ν_{CPMG}, the RF strength ν_1, and the ^{15}N carrier position.

3.2.3 $^{15}N_\varepsilon$ Relaxation Analysis Using Direct $^{13}C_\zeta$ Detection—

Hansen and coworkers analyzed Arg side-chain $^{15}N_\varepsilon$ relaxation through direct detection of $^{13}C_\zeta$ nuclei (Werbeck, Kirkpatrick, & Hansen, 2013). A remarkable advantage of this approach is that it can be used at any pH because rapid hydrogen exchange does not impact $^{13}C_\zeta$ detection. In fact, this method was successfully applied to a 42-kDa protein at pH 8.2. ^1H detection of Arg side-chain $N_\varepsilon H$ groups at this pH is virtually impossible due to the rapid hydrogen exchange with water. Because the $^{13}C_\zeta$ resonances are unaffected by hydrogen exchange, $^{15}N_\varepsilon$ relaxation analysis through direct $^{13}C_\zeta$ detection is possible. A drawback of this method is that it provides relaxation rates for $2C_zN_x$ and $2C_zN_z$ terms but not those for N_x and N_z terms. Werbeck et al. demonstrated that the order parameters determined using this method agree well with those determined using the standard ^{15}N relaxation method.

3.3 Determination of Lys/Arg Side-Chain Order Parameters

3.3.1 Overall Procedures—

The ^{15}N relaxation data for Lys and Arg side chains at multiple magnetic fields are used to calculate order parameters for relevant bonds. The overall procedures for this calculation are shown in Fig. 6A. To determine the order parameter and the correlation times for internal motions, the following function is minimized for each side chain:

$$\chi^2 = \sum_{Type} \sum_{Field} \frac{(Y_{obs} - Y_{cal})^2}{w^2}, \quad (2)$$

where Y_{obs} and Y_{cal} stand for the observed and calculated quantities. The squared difference terms are summed for different types of relaxation parameters (i.e., R_1, R_2, and NOE) and for different magnetic fields. The use of multiple magnetic fields is important because up to three parameters for internal motions are optimized. Based on availability of our NMR spectrometers, we typically combine ^{15}N relaxation data at 600 and 800 MHz for Lys NH_3^+ groups, and combine those at 600 and 750 MHz for Arg $N_\varepsilon H$ groups. In Eq. (2), $1/w^2$ corresponds to the weight of each squared difference $(Y_{obs} - Y_{cal})^2$. For this kind of fitting calculation, two different weights have been used: $w = Y_{obs}$ (e.g., Dellwo & Wand, 1989; Nicholson et al., 1992) or $w = \sigma$, where σ represents the uncertainty in Y_{obs} (e.g., Mandel, Akke, & Palmer, 1995; Palmer, Rance, & Wright, 1991). Although the latter approach may seem to be more reasonable, it is not necessarily the case when there is bias causing a large systematic error in Y_{obs} that deviates from the true value. An example of such bias is on NOE data impacted by the saturation transfer effect (Grzesiek & Bax, 1993; Li & Montelione, 1994). The approach using $w = Y_{obs}$ is safer if some systematic errors may exist in the experimental data. Calculation of Y_{cal} requires the use of an appropriate spectral density function relevant to the ^{15}N relaxation parameters. The parameters involved in the spectral density function are optimized through minimization of the sum of the squared differences represented by Eq. (2).

3.3.2 Determination of Molecular Rotational Correlation Time—Calculation of Y_{cal} in Eq. (2) requires the molecular rotational correlation time. However, the ^{15}N relaxation data of Lys and Arg side chains are not suitable for determination of the molecular rotational correlation time because many Lys and Arg side chains are highly flexible and internal motions govern the ^{15}N relaxation parameters. Therefore, the molecular rotational correlation time is determined using backbone ^{15}N R_1 and R_2 relaxation data for rigid regions of the same protein under the identical conditions. For calculations of rotational diffusion anisotropy, the atomic coordinates of the 3D structure are also required. In many cases, the axially symmetric diffusion model (Woessner, 1962) is suitable for the rotational diffusion calculation. Through nonlinear least-squares fitting, rotational diffusion parameters ($D_\parallel$, $D_\perp$, and two polar angles for the main principal axis) for the axially symmetric diffusion model are determined from the R_1/R_2 ratio data for backbone ^{15}N nuclei (Tjandra, Feller, Pastor, & Bax, 1995). For this calculation, we use a C program (Iwahara, Peterson, & Clubb, 2005). The effective rotational correlation time $\tau_{r,eff}$ and the anisotropy of the rotational diffusion r are given by $(2D_\parallel + 4D_\perp)^{-1}$ and $D_\parallel/D_\perp$, respectively (Woessner, 1962). The effective rotational correlation time $\tau_{r,eff}$ is used as a fixed-value parameter to calculate Y_{cal} when Lys/Arg side-chain order parameters are determined through minimization of Eq. (2).

3.3.3 Determination of Lys NH_3^+ Order Parameters—The spectral density function for dipole–dipole (DD) autorelaxation of the ^{15}N nucleus in an NH_3^+ group is given by (Esadze et al., 2011):

$$j_{DD}(\omega) = \frac{\zeta^2}{4\pi}\left[\frac{(1/9)S^2_{axis}\tau_m}{1+\omega^2\tau_m^2} + \frac{(8/9)S^2_{axis}\tau_1}{1+\omega^2\tau_1^2} + \frac{(1/9)\left(1-S^2_{axis}\right)\tau_2}{1+\omega^2\tau_2^2} + \frac{(8/9)\left(1-S^2_{axis}\right)\tau_3}{1+\omega^2\tau_3^2}\right] \quad (3)$$

where $\zeta = \sqrt{(6\pi/5)}(\mu_0/4\pi)(h/2\pi)\gamma_H\gamma_N r_{NH}^{-3}$; μ_0, the vacuum permeability; h, Planck's constant; γ, the nuclear gyromagnetic ratio; r_{ij}, the N–H distance; S^2_{axis}, the generalized order parameter for the symmetry axis of the NH_3^+ group; τ_m, the overall molecular rotational correlation time; $\tau_1^{-1} - = \tau_m^{-1} + \tau_f^{-1}$; $\tau_{2-1} = \tau_m^{-1} + \tau_i^{-1}$; $\tau_{3-1} = \tau_m^{-1} + \tau_f^{-1} + \tau_i^{-1}$; τ_i, the correlation time for reorientation of the symmetry axis; and τ_f, the correlation time for bond rotation around the symmetry axis. Fig. 8B depicts the physical meanings of the parameters S^2_{axis}, τ_f, and τ_i. The spectral density function of Eq. (3) is a modification of Eq. (15) of Kay and Torchia (1991) for CH_3 groups, and is derived from the product of correlation functions for overall motions, internal motions of symmetry axis, and bond rotation (Esadze et al., 2011). The total number of parameters involved is identical for these equations and if $\tau_i \gg \tau_f$, the equations become the same. Eq. (3) is more general because it is applicable even when the inequality $\tau_i \gg \tau_f$ does not hold. This aspect of Eq. (3) is important because hydrogen bonds may slow down the bond rotation and make $\tau_i < \tau_f$. The ^{15}N relaxation through CSA is negligible because $|\sigma_\parallel - \sigma_\perp|$ is as small as 15 ppm for Lys NH_3^+ groups (Sarkar et al., 1987). With the spectral density function $j_{DD}(\omega)$, the ^{15}N relaxation parameters of the NH_3^+ group are given by:

$$R_1 = 3j_{DD}(\omega_N) + 6j_{DD}(\omega_H + \omega_N) + j_{DD}(\omega_H - \omega_N) \quad (4)$$

$$R_{2,ini} = 2j_{DD}(0) + (3/2)j_{DD}(\omega_N) + 3j_{DD}(\omega_H + \omega_N) + 3j_{DD}(\omega_H) + (1/2)j_{DD}(\omega_H - \omega_N) \quad (5)$$

$$NOE = 1 + (\gamma_H/\gamma_N)(6j_{DD}(\omega_H + \omega_N) - j_{DD}(\omega_H - \omega_N))/R_1, \quad (6)$$

For calculations of the order parameters and the internal motion correlation times for Lys NH_3^+ groups, the complete source code of the Mathematica® script is available in the supporting information of Esadze et al. (2011). This script does not take the anisotropy of molecular rotational diffusion into consideration because the rotational anisotropy exerts only very minor effects on $^{15}NH_3^+$ relaxation, as is evident from Eq. (6) of Tjandra et al. (1995) and the small overall order parameters (i.e., $S^2_{axis}/9$) for NH_3^+ groups.

3.3.4 Determination of Arg $N_\varepsilon H$ Order Parameters—

Since each Arg side-chain $^{15}N^1_\varepsilon H$ group can be regarded as an AX spin system, the relaxation parameters of Arg $^{15}N_\varepsilon$ nuclei can be analyzed using the same equations as those for backbone ^{15}N nuclei. Therefore, computer programs to calculate the order parameters and the correlation times for the internal motions of backbone NH groups [e.g., the ModelFree program by Palmer

(Mandel et al., 1995); the Mathematica® script by Spyracopoulos (Spyracopoulos, 2006)] can be used to compute the corresponding model-free parameters for Arg $N_\varepsilon H$ groups. However, it should be noted that different settings are required for the ^{15}N CSA values and the ^{15}N–^{1}H distance r_{NH} of Arg side-chain $N_\varepsilon H$ groups: $|\sigma_\parallel - \sigma_\perp| = 114$ ppm and $r_{NH} = 1.04$ Å should be used for Arg side-chain $^{15}N_\varepsilon$ nuclei (Trbovic et al., 2009), whereas $|\sigma_\parallel - \sigma_\perp| = 170$ ppm and $r_{NH} = 1.02$ Å are typically used for backbone ^{15}N nuclei (Tjandra, Szabo, & Bax, 1996).

3.3.5 Different Dynamic Properties of Lys and Arg Side Chains—

To show typical ranges of Lys/Arg side-chain order parameters, the data for the Lys and Arg side chains of the Antp homeodomain and the Egr-1 zinc-finger protein in the free and DNA-bound states are shown in Fig. 7. Note that the order parameters S^2_{axis} of Lys NH_3^+ groups are defined for the C_3 symmetry axis, which corresponds to the C_ε–N_ζ bond. Although the same number of rotatable bonds (i.e., four covalent bonds) is involved between Lys C_α and C_ε atoms and between Arg C_α and N_ε atoms, the ranges of the measured order parameters were remarkably different for Lys C_ε–N_ε and Arg N_ε–H_ε bonds. Compared to Lys C_ε–N_ε bonds, Arg N_ε–H_ε bonds exhibited a wider range of order parameters as well as larger changes in order parameters upon binding to DNA. The mobility of Arg side chains seems to be more sensitive to the surrounding environment, compared to Lys side chains.

3.4 $^3J_{CN}$ Measurements to Analyze Side-Chain Dynamics

Three-bond *J*-coupling data reflect the dynamics of torsion angles (Chou, Case, & Bax, 2003; Perez, Löhr, Rüterjans, & Schmidt, 2001; Zandarashvili et al., 2011). Those between ^{15}N and ^{13}C nuclei are relatively easy to measure using quantitative *J*-modulation experiments. The spin-echo *J*-modulation constant-time HSQC or HNCG experiments (Hu & Bax, 1997) can be used to measure the $^3J_{NC}$ couplings between backbone ^{15}N and side-chain $^{13}C_\gamma$ nuclei relevant to χ_1 angles of Lys and Arg side chains and other side chains. For $^3J_{CN}$ couplings between Lys $^{13}C_\gamma$ and $^{15}N_\zeta$ nuclei relevant to χ_4 angles can be measured through the spin-echo $^3J_{CN}$-modulation constant-time HISQC experiment selective for NH_3^+ groups (Zandarashvili et al., 2011). The $^3J_{CN}$ coupling constants are typically less than 0.5–3 Hz. The precision of the measured coupling constants $^3J_{CN}$ relevant to χ_4 angles is high owing to the very slow ^{15}N relaxation of the Lys NH_3^+ groups allowing the use of a long period for *J*-modulation. $^3J_{CN}$ data can be interpreted by means of the Karplus equation (Karplus, 1959) together with empirical parameters (see Section 5.1). Due to the conformational fluctuation, the experimental $^3J_{NC}$ data agree better with those predicted from MD trajectories than with those calculated from crystal structures (see Section 5.1).

4. ION PAIRS AND HYDROGEN BONDS INVOLVING Lys/Arg SIDE CHAINS

NMR studies of Lys and Arg side chains provide unique information on electrostatic interactions, hydrogen bonds, and their dynamics. Recent NMR studies illuminated the dynamic nature of short-range electrostatic interactions via ion pairs (also known as salt bridges).

4.1 Hydrogen-Bond Scalar Couplings

4.1.1 Heteronuclear Correlation via Hydrogen-Bond Scalar Couplings—

Hydrogen-bond scalar couplings reflect the orbital overlaps in hydrogen bonds and provide unique information about hydrogen bonding (Grzesiek, Cordier, Jaravine, & Barfield, 2004). Hydrogen-bond scalar couplings provide direct evidence of hydrogen bonds and, in fact, are included in IUPAC's recently updated criteria for hydrogen bonds (Arunan et al., 2011). Hydrogen-bond scalar couplings can also provide information about dynamics because these couplings are influenced by the transient distortion or breakage of the hydrogen bonds as well (Jaravine, Alexandrescu, & Grzesiek, 2001; Markwick, Sprangers, & Sattler, 2003; Zandarashvili et al., 2016, 2011).

Owing to the very slow ^{15}N transverse relaxation of NH_3^+ groups, which permits the use of a long period for *J*-modulation, hydrogen-bond scalar coupling constants in the range of 0.1–1.0 Hz can readily be measured for Lys side chains of midsize (~30kDa) systems studied by NMR. This allows direct detection and characterizations of hydrogen bonds involving Lys NH_3^+ by NMR. Fig. 8A and B shows the NMR pulse sequences for observing ^{15}N–^{13}C or ^{15}N–^{31}P scalar couplings across hydrogen bonds involving Lys NH_3^+ groups (Anderson et al., 2013; Zandarashvili et al., 2011). The F_2 dimension corresponds to ^{1}Hζ resonances of the NH_3^+ groups, and the F_1 dimension corresponds to ^{13}C or ^{31}P resonances of nuclei coupled to Lys ^{15}Nζ. Some examples are shown in Fig. 8E and F. The $^{h3}J_{NP}$ couplings with DNA phosphate ^{31}P nuclei were observed for the interfacial Lys side chains of several protein–DNA complexes (Anderson et al., 2013, 2015; Chen et al., 2015; Esadze et al., 2016; Zandarashvili, Esadze, et al., 2015; Zandarashvili, Nguyen, et al., 2015).

4.1.2 Determination of Hydrogen-Bond Scalar Coupling Constants—

Although the abovementioned heteronuclear correlation spectra via hydrogen-bond scalar couplings are useful to identify the acceptor groups for the hydrogen bonds of Lys NH_3^+ groups, these spectra do not provide quantitative information on the hydrogen-bond scalar couplings. The values of $|^{h3}J_{NC}|$ or $|^{h3}J_{NP}|$ can be determined using the spin-echo ^{h3}J-modulation constant-time HISQC experiments selective for NH_3^+ groups (Fig. 8C and D) (Anderson et al., 2013; Zandarashvili et al., 2011). In these experiments, two subspectra are recorded in an interleaved manner: one with the ^{13}C or ^{31}P 180° pulses at position a (subspectrum *a*) and the other at position *b* (subspectrum *b*). The values of $|^{h3}J|$ can be calculated from $I_a/I_b = \cos 2\pi J(T_d + \delta)$, in which I_a and I_b represent signal intensities in subspectra *a* and *b*, respectively. For $^{h3}J_{NP}$ coupling, we use a cryogenic ^{1}H/^{13}C/^{15}N/^{31}P QCI probe (Bruker) operated at the ^{1}H frequency of600 MHz. This probe is well suited to study hydrogen-bond scalar couplings involving DNA/RNA ^{31}P nuclei. Using this probe, we were also able to observe $^{h3}J_{NP}$ and $^{h2}J_{HP}$ couplings between zinc-coordinating His side-chain ^{1}H/^{15}N and DNA phosphate ^{31}P nuclei in the Egr-1 zinc-finger–DNA complex as well (Chattopadhyay, Esadze, Roy, & Iwahara, 2016).

4.2 Dynamic Ion Pairs and Hydrogen Bonds

4.2.1 Dynamic Hydrogen Bonding and Ion Pairing—

Although one may expect that side chains forming hydrogen bonds and/or ion pairs could be immobilized, recent NMR data show that this situation is not always the case for basic side chains (Anderson et al.,

2013; Chen et al., 2015; Esadze et al., 2016; Nguyen, Hoffpauir, et al., 2017; Trbovic et al., 2009; Zandarashvili et al., 2011). Hydrogen bonds involving basic side chains can rapidly break and form, depending on the energy barriers involved. If the breakage and formation of hydrogen bonds occur on a picosecond–nanosecond timescale, the NMR order parameters and internal motion correlation times reflect the hydrogen-bond dynamics. A recent NMR study on the temperature dependence of the Lys side-chain ^{15}N relaxation suggested that the free energy of activation ($\Delta G^{\ddagger}$) is as small as 2–5 kcal/mol for breaking hydrogen bonds of Lys NH_3^+ groups, though the enthalpy of activation ($\Delta H^{\ddagger}$) is as large as 5–14kcal/mol (Zandarashvili & Iwahara, 2015). Recent NMR studies showed that the Lys NH_3^+ groups interacting with DNA phosphate groups exhibit small order parameters ($S^2_{axis} < 0.5$) and sizable $^{h3}J_{NP}$ couplings, indicating the coexistence of high mobility and hydrogen bonding (Anderson et al., 2013; Chen et al., 2015; Esadze et al., 2016; Nguyen, Hoflpauir, et al., 2017). This somewhat puzzling behavior can be understood in terms of the dynamic equilibrium between the contact ion-pair (CIP) and solvent-separated ion-pair (SIP) states (Iwahara, Esadze, & Zandarashvili, 2015), as described in Section 5.2. It should be noted that the CIP–SIP transitions do not decouple (but do attenuate) the $^{h3}J_{NP}$ couplings between the Lys ^{15}N and DNA ^{31}P nuclei as long as the $|\alpha\rangle$ or $|\beta\rangle$ spin states of the coupled ^{31}P nuclei are largely maintained during the $^{h3}J_{NP}$ evolution period for the ^{15}N coherence. Small order parameters of the interfacial Lys NH_3^+ groups can also be explained by the CIP–SIP transitions occurring on a pico-to-nanosecond timescale, as suggested by MD simulations (Chen et al., 2015; Esadze et al., 2016).

4.2.2 Self-decoupling Due to Molecular Dissociation—

Hydrogen-bond scalar couplings are very useful data that represent direct evidence of hydrogen bonds. However, it should be noted that the intermolecular hydrogen-bond scalar couplings between two molecules can be observed only when the residence time of the complex is sufficiently long. When the residence time is shorter than or comparable to $1/(\pi^h J)$, the self-decoupling effect makes the apparent coupling constant smaller than $^h J$. We recently studied the self-decoupling effect theoretically and experimentally (Zandarashvili et al., 2016). Self-decoupling is easy to qualitatively understand. Consider a protein side-chain ^{15}N nuclei coupled to DNA phosphate ^{31}P nuclei for example. In solution, the protein can dissociate from a DNA molecule and associate with another DNA molecule of the same kind. When this happens, the spin state of the interacting ^{31}P nuclei can change from $|\alpha\rangle$ to $|\beta\rangle$ or vice versa. Therefore, rapid translocation of the protein effectively mixes the $|\alpha\rangle$ to $|\beta\rangle$ spin states of the coupled ^{31}P nuclei and causes decoupling of $^{h3}J_{NP}$ for protein ^{15}N nuclei. A Liouville equation description allows the self-decoupling effect of intermolecular hydrogen-bond scalar coupling to be quantitatively analyzed and gain information about the residence time of macromolecular complexes. This approach was demonstrated for intermolecular hydrogen-bond scalar couplings between Lys side-chain ^{15}N and DNA ^{31}P nuclei measured for protein–DNA complexes at various ionic strengths (Zandarashvili et al., 2016). The self-decoupling-based method is unique in that it does not require different chemical shifts for the interconverting states, while such conditions are crucial for other NMR methods for kinetic investigations of protein–DNA interactions (Iwahara, Zandarashvili, Kemme, & Esadze, 2018). Although self-decoupling is typically regarded as a nuisance in NMR scalar coupling measurements (Cavanagh et al., 2007; Harbison, 1993; Kuboniwa, Grzesiek,

Delaglio, & Bax, 1994), the quantitative analysis of self-decoupling presents a useful tool for kinetic investigations of processes that accompany breakage of intermolecular hydrogen bonds.

5. DATA INTERPRETATION FACILITATED BY MOLECULAR DYNAMICS SIMULATIONS

NMR spectroscopy can provide atomic-level information about the structures and dynamics of proteins and their complexes, but experimental data are available only for particular analyzable atoms of proteins. In contrast, MD simulations can give information on all atoms of the system including solvent molecules and free ions, but the computational studies are based on empirical models that need experimental validation, especially for electrostatic interactions. NMR and MD are complementary in this sense. MD simulations have greatly facilitated the interpretation of NMR data on basic side chains and their electrostatic interactions (Chen et al., 2015; Esadze et al., 2016, 2011; Trbovic et al., 2009; Zandarashvili et al., 2011). In what follows, we describe how MD simulations can facilitate the interpretation of NMR data on basic side chains.

5.1 NMR vs MD for Dynamics of Basic Side Chains

5.1.1 Lys/Arg Side-Chain Order Parameters From MD Trajectories—The calculation of order parameters from MD trajectories and comparison of experimental and computational order parameters have been conducted since 1980s (Chatfield, Szabo, & Brooks, 1998; Levy et al., 1985; Lipari, Szabo, & Levy, 1982). However, it is only recently that NMR- and MD-derived order parameters were compared for cationic moieties of basic side chains (Chen et al., 2015; Esadze et al., 2016, 2011; Trbovic et al., 2009). For such comparison, the behavior of Lys C_ε–N_ζ and Arg N_ε–H_ε bonds in the MD trajectories should be analyzed. Lys C_ε–N_ζ bonds are used because the NMR order parameter for each Lys side-chain NH_3^+ is defined for its symmetry axis.

The dynamic behavior of a bond vector from MD trajectories can be studied by calculating the autocorrelation function for internal motions $C_I(t)$. This function is given by (Case, 2002; Lipari & Szabo, 1982):

$$C_I(t) = \langle P_2(\mu(t_0)\mu(t_0 + t))\rangle, \tag{7}$$

where $\mu(t_0)\mu(t_0+t)$ is the projection of a unit vector pointing along a bond vector at time t_0 onto itself at time $t_0 + t$; $P_2(x) = (3x^2 - 1)/2$ is the second Legendre polynomial; and the brackets denote a time average over the trajectory. The trajectory frames are superimposed onto an optimal (in the least squares sense) common reference frame to remove the effects of overall tumbling and translation. Then, the time dependence of the autocorrelation for the reorientational motion is better described in Clore's extended model-free formulism (Clore et al., 1990):

$$C_I(t) = S^2 + \left(1 - S_f{}^2\right)\exp\left(-t/\tau_f\right) + \left(S_f{}^2 - S^2\right)\exp\left(-t/\tau_i\right), \tag{8}$$

where S_f^2 and τ_f correspond to the amplitude and correlation time due to fast librational motion; and S^2 and τ_i are the order parameter and correlation time of the reorientational motion of a bond vector. Using a single exponential in the case of methyl group dynamics is often satisfactory (Frederick, Sharp, Warischalk, & Wand, 2008), while for the more chemically complex basic side chains, we found that method of analysis gave poor results. The implication is that these side chains have a rich dynamical range of motion and are strongly coupled to their surroundings with varied time scales. Some $C_I(t)$ functions calculated for the Lys C_ε–N_ζ and Arg N_ε–H_ε bonds of the Egr-1 zinc-finger protein bound to its target DNA are shown in Fig. 9A. Use of sufficiently long (on μs order) MD trajectories is important for accurate computation of the order parameters (Bowman, 2016). This seems to be particularly important for the analysis of Arg side chains because we noticed that the $C_I(t)$ functions for Arg N_ε–H_ε bonds tend to exhibit slow convergence or decay.

The correlation between the NMR and MD order parameters for the Lys and Arg side chains of the Egr-1 zinc-finger protein bound to its target DNA is shown in Fig. 9B. In general, the order parameters calculated from MD trajectories tend to be smaller than the NMR-derived order parameters, as pointed out by Brüschweiler and coworkers (Gu, Li, & Brüschweiler, 2014). This is because the impact of $C_I(t)$ on the overall correlation function relevant to NMR relaxation is scaled by $\exp(-t/\tau_r)$ (Lipari & Szabo, 1982), thereby making NMR data insensitive to motions on a 10^{-8}–10^{-6}s timescale. Since τ_r is typically 5–50ns for most proteins analyzed by NMR, an order parameter as a plateau of $C_I(i)$ beyond 50 ns has only little impact on NMR relaxation. In addition, depending on the details of the system, some find consistent estimates of S^2 from different force fields (Bowman, 2016), while the details of methyl dynamics can display more variations (O'Brien et al., 2016). Nevertheless, significant correlations have been found between the NMR and MD order parameters for Arg/Lys side chains (Chen et al., 2015; Esadze et al., 2016, 2011; Trbovic et al., 2009). These correlations with the experimental data validate MD-based investigations into the properties of basic side chains that are difficult to assess by NMR (see Sections 5.2 and 5.3).

5.1.2 Three-Bond Scalar Couplings From MD Trajectories—The dihedral angles χ of long side chains can dynamically change through conformational fluctuations. Three-bond $^3J_{NC}$ coupling constants relevant to Lys and Arg side-chain χ angles can be measured through spin-echo $^3J_{NC}$ modulation experiments, as described in Section 3.4. The three-bond coupling constants can directly be compared with those predicted from MD trajectories. This analysis utilizes the Karplus equation (Karplus, 1959) for the relationship between the $^3J_{NC}$ coupling constant and the dihedral angle χ between the coupled ^{15}N and ^{13}C nuclei:

$$^3J_{NC} = A\cos^2\chi + B\cos\chi + C \quad (9)$$

The parameters A, B, and C are empirically determined, for example, $A = 1.29$, $B = -0.49$, and $C = 0.37$ for χ_1 angles (Perez et al., 2001) and $A = 1.29$, $B = -0.49$, and $C = 0.63$ for Lys χ_4 angles (Huang & MacKerell, 2013). Ensemble averages, $\langle^3J_{NC}\rangle$, are calculated from χ angles in numerous snapshots sampled from MD trajectories. Interestingly, experimental $^3J_{NC}$ data tend to exhibit far better correlation with the $\langle^3J_{NC}\rangle$ data predicted from the MD

ensemble than with those predicted from the crystal structure (Chen et al., 2015; Zandarashvili et al., 2011), as shown in Fig. 10. These results suggest that the χ torsion angles of these side chains are actually as dynamic as seen in the MD simulation. Thus, $^{3}J_{NC}$ data can also illuminate the dynamic nature of basic side chains.

5.2 Ion-Pair Dynamics in MD Simulations

Ion pairs with charged side chains can involve both strong short-range electrostatic interactions and hydrogen bonds. Although the NMR data of hydrogen-bond scalar couplings ($^{h3}J_{NP}$) between protein ^{15}N and DNA ^{31}P nuclei indicate the presence of hydrogen bonds in the intermolecular ion pairs, the NMR S^2 and $^{3}J_{NC}$ data clearly indicate that the Lys side chains interacting with DNA phosphates are highly mobile (Anderson et al., 2013; Chen et al., 2015). How can the Lys side-chain NH_3^+ groups exhibit high mobility despite the simultaneous presence of hydrogen bonds and strong short-range attractive electrostatic interactions? While the answer to this question was not immediately obvious from the NMR investigations alone, MD simulations provided useful insight into this question and facilitated interpretation of the NMR data.

5.2.1 Analysis of CIP–SIP Transitions—The dynamic behavior of biomolecular ion pairs becomes evident through analysis of the distances between cationic and anionic moieties in MD trajectories. Fig. 11A shows the N…O distances from the interfacial Lys side-chain NH_3^+ group to the closest DNA phosphate in the 0.6-μs MD trajectories for the Antp homeodomain–DNA complex and the Egr-1 zinc-finger–DNA complex (Chen et al., 2015). These N…O distances dynamically fluctuated between two ranges: one between 2.5 and 3.2 Å, corresponding to the CIP states, and the other between 3.8 and 6.0 Å, corresponding to the SIP states. The transitions between the CIP and SIP states occurred on a pico-to-nanosecond timescale. This dynamic behavior of biomolecular ion pairs is reasonable in light of the fundamental concepts that were established for small ions over the last several decades (Fennell, Bizjak, Vlachy, & Dill, 2009; Marcus & Hefter, 2006; Masnovi & Kochi, 1985; Masunov & Lazaridis, 2003; Peters & Li, 1994; Pettitt & Rossky, 1986; Szwarc, 1972). The order parameters S^2_{axis} and $^{3}J_{N\zeta C\gamma}$ coupling constants predicted from the MD trajectories were consistent with experimental data from NMR experiments. The CIP–SIP transitions make the interfacial Lys side chains highly dynamic, making the order parameters small, whereas the major presence of CIP causes sizable hydrogen-bond scalar couplings $^{h3}J_{NP}$.

5.2.2 Free-Energy Analysis of the CIP–SIP Equilibria—MD trajectories enable calculations of the potentials of mean force (PMFs) for these ion pairs. PMFs represent the effective potential or free-energy landscapes given as a function of the interionic distance. Fig. 11C shows the PMFs as a function the N…O distance (r_{NO}) for the ion pairs of the Lys side-chain NH_3^+ and DNA phosphate groups (Chen et al., 2015). These PMFs were obtained though analysis of the probability distribution $p(r_{NO})$ (Fig. 11B), which is based on a histogram of the r_{NO} values in the MD trajectory. The free energy is calculated as $G = -RT \ln p(r_{NO})$, where R is the gas constant; T is the standard temperature (i.e., $T = 298.15$ K). The two minima in PMFs correspond to the CIP and SIP states. The peak between these states corresponds to the effective free energy barrier for the CIP–SIP transition, provided

that the PMFs represent the reaction coordinates. With a higher energy barrier, the CIP–SIP transitions should be slower. For the protein–DNA ion pairs whose CIP states were experimentally detected, the free energy differences between CIP and SIP states were determined to be 0.8–1.6 kcal/mol. The energy barriers for CIP → SIP transitions were determined to be 2.2–3.2kcal/mol, which are qualitatively consistent with the mean lifetimes of the CIP states. The relatively small free energy difference between CIP and SIP as well as the low-energy barrier between these states can explain the highly dynamic nature of the interfacial ion pairs involving Lys side chains.

5.3 Conformational Entropy of Basic Side Chains

Changes in the conformational entropies of protein side chains can make significant contribution to the overall change in free energy upon molecular association (Wand, 2013; Wand & Sharp, 2018). Because basic side chains are important constituents of electrostatic interactions in molecular recognition by proteins, the conformational entropies of these side chains are of particular interest. For CH_3-containing side chains, the order parameters S^2_{axis} for CH_3 groups are used as "meters" of side-chain conformational entropy (Kasinath, Sharp, & Wand, 2013; Li & Brüschweiler, 2009). For Lys and Arg side chains, however, the order parameters of their cationic groups do not necessarily serve as good meters of the conformational entropy of the entire side chain because CH_2 moieties could remain flexible even if the cationic moieties are restricted by hydrogen bonds (Li & Brüschweiler, 2009; Trbovic et al., 2009). Lys and Arg side-chain conformational entropies can be calculated from the distributions of the dihedral angles sampled during an MD simulation (Karplus & Kushick, 1981; Trbovic et al., 2009):

$$S = -R\int P\left(\vec{\chi}\right)\ln P\left(\vec{\chi}\right)\mathrm{d}\vec{\chi}, \tag{10}$$

where R is the gas constant and $P(\vec{\chi})$ is the probability density as a function of the dihedral angles χ_1, χ_2, χ_3, and χ_4 of each Arg or Lys side chain. We tested the dependence of the entropies on the bin size of the integral mesh and chose 5° (Esadze et al., 2016). The bin size of the integral mesh affects the absolute entropy but, given reasonable resolution, does not affect the change in conformational entropy. Fig. 12A displays the change in conformational entropy of each Arg/Lys side chain of the Egr-1 zinc-finger protein upon binding to its target DNA, which was calculated from the MD trajectories using Eq. (10) (Esadze et al., 2016). Fig. 12B shows the correlation between the changes in the NMR-derived order parameters of the Lys NH_3^+ and Arg $N_\varepsilon H$ groups and the changes in the MD-derived conformational entropy of the same side chains upon complex formation.

6. CONCLUDING REMARKS

NMR experiments on Lys and Arg side chains can provide unique insights into their conformational dynamics, hydrogen bonds, and electrostatic interactions. Functionally important Lys and Arg side chains tend to show relatively slow hydrogen exchange due to hydrogen bonding, which facilitates NMR-based characterizations of these side chains. For the NMR experiments to work, optimization of pH and temperature can be necessary so that hydrogen exchange becomes slow enough to detect ^1H signals from the cationic groups. The

intrinsic ^{15}N transverse relaxation of Lys NH_3^+ groups is very slow, which makes it possible to precisely measure small scalar couplings, including those across hydrogen bonds. The pulse programs and parameter sets for the pulse sequences introduced in this chapter are available upon request at our laboratory website (https://scsb.utmb.edu/labgroups/iwahara/software/).

ACKNOWLEDGMENTS

This work was supported by Grant CHE-1608866 from the National Science Foundation (to J.I.) and partly by Grants R01-GM066813 (to B.M.P.) and R01-GM037657 (to B.M.P.). D.N. is a recipient of the Houston Area Molecular Biophysics Program fellowship (supported by NIH Grant T32-GM008280).

REFERENCES

Abragam A (1961). Thermal relaxation in liquids and gases In The principle of nuclear magnetism (pp. 264–353). Oxford: Carendon Press.

Aeby N, & Bodenhausen G (2008). Determination of transverse relaxation rates of individual spins while quenching echo modulations due to homonuclear scalar couplings. Chemical Physics Letters, 463(4–6), 418–421.

Anderson KM, Esadze A, Manoharan M, Brüschweiler R, Gorenstein DG, & Iwahara J (2013). Direct observation of the ion-pair dynamics at a protein-DNA interface by NMR spectroscopy. Journal of the American Chemical Society, 135(9), 3613–3619. [PubMed: 23406569]

Anderson KM, Nguyen D, Esadze A, Zandrashvili L, Gorenstein DG, & Iwahara J (2015). A chemical approach for site-specific identification of NMR signals from protein side-chain NH_3^+ groups forming intermolecular ion pairs in protein-nucleic acid complexes. Journal of Biomolecular NMR, 62(1), 1–5. [PubMed: 25690740]

Andre I, Linse S, & Mulder FA (2007). Residue-specific pKa determination of lysine and arginine side chains by indirect ^{15}N and ^{13}C NMR spectroscopy: Application to apo calmodulin. Journal of the American Chemical Society, 129(51), 15805–15813. [PubMed: 18044888]

Arunan E, Desiraju GR, Klein RA, Sadlej J, Scheiner S, Alkorta I, et al. Nesbitt DJ, (2011). Definition of the hydrogen bond (IUPAC Recommendations 2011). Pure and Applied Chemistry, 83(8), 1637–1641.

Baldwin AJ, Hansen DF, Vallurupalli P, & Kay LE (2009). Measurement of methyl axis orientations in invisible, excited states of proteins by relaxation dispersion NMR spectroscopy. Journal of the American Chemical Society, 131(33), 11939–11948. [PubMed: 19627152]

Bax A, Ikura M, Kay LE, Torchia DA, & Tschudin R (1990). Comparison of different modes of two-dimensional reverse-correlation NMR for the study of proteins. Journal of Magnetic Resonance, 86, 304–318.

Blaum BS, Deakin JA,Johansson CM, Herbert AP, Barlow PN, Lyon M,et al. (2010). Lysine and arginine side chains in glycosaminoglycan-protein complexes investigated by NMR, cross-linking, and mass spectrometry: A case study of the factor H-heparin interaction. Journal of the American Chemical Society, 132(18), 6374–6381. [PubMed: 20394361]

Boehr DD, Dyson HJ, & Wright PE (2006). An NMR perspective on enzyme dynamics. Chemical Reviews, 106(8), 3055–3079. [PubMed: 16895318]

Bowman GR (2016). Accurately modeling nanosecond protein dynamics requires at least microseconds of simulation. Journal of Computational Chemistry, 37(6), 558–566. [PubMed: 26077712]

Bunker BC (1994). Molecular mechanisms for corrosion of silica and silicate-glasses. Journal of Non-Crystalline Solids, 179, 300–308.

Carr HY, & Purcell EM (1954). Effects of diffusion on free precession in nuclear magnetic resonance experiments. Physics Review, 94, 630–638.

Case DA (2002). Molecular dynamics and NMR spin relaxation in proteins. Accounts of Chemical Research, 35(6), 325–331. [PubMed: 12069616]

Cavanagh J, Fairbrother WJ, Palmer AG III, Rance M, & Skelton NJ (2007). Chemical exchange effects in NMR spectroscopy protein NMR spectroscopy: Principles and practice (2nd ed., pp. 391–402).Burlignton: Elsevier, Academic Press.

Chatfield DC, Szabo A, & Brooks BR (1998). Molecular dynamics of staphylococcal nuclease: Comparison of simulation with ^{15}N and ^{13}C NMR relaxation data. Journal of the American Chemical Society, 120(21), 5301–5311.

Chattopadhyay A, Esadze A, Roy S, & Iwahara J (2016). NMR scalar couplings across intermolecular hydrogen bonds between zinc-finger histidine side chains and DNA phosphate groups. The Journal of Physical Chemistry. B, 120, 10679–10685. [PubMed: 27685459]

Chen CY, Esadze A, Zandarashvili L, Nguyen D, Pettitt BM, & Iwahara J (2015). Dynamic equilibria of short-range electrostatic interactions at molecular interfaces of protein-DNA complexes. Journal of Physical Chemistry Letters, 6(14), 2733–2737.

Chou JJ, Case DA, & Bax A (2003). Insights into the mobility of methyl-bearing side chains in proteins from $^{3}J_{CC}$ and $^{3}J_{CN}$ couplings. Journal of the American Chemical Society, 125(29), 8959–8966. [PubMed: 12862493]

Clore GM, & Gronenborn AM (1998). Determining the structures of large proteins and protein complexes by NMR. Trends in Biotechnology, 16(1), 22–34. [PubMed: 9470228]

Clore GM, & Iwahara J (2009). Theory, practice, and applications of paramagnetic relaxation enhancement for the characterization of transient low-population states of biological macromolecules and their complexes. Chemical Reviews, 109(9), 4108–4139. [PubMed: 19522502]

Clore GM, Szabo A, Bax A, Kay LE, Driscoll PC, & Gronenborn AM (1990). Deviations from the simple 2-parameter model-free approach to the interpretation of ^{15}N nuclear magnetic-relaxation of proteins. Journal of the American Chemical Society, 112(12), 4989–4991.

Dellwo MJ, & Wand AJ (1989). Model-independent and model-dependent analysis of the global and internal dynamics of cyclosporine-A. Journal of the American Chemical Society, 111(13), 4571–4578.

Dittmer J, & Bodenhausen G (2006). Quenching echo modulations in NMR spectroscopy. Chemphyschem, 7(4), 831–836. [PubMed: 16528781]

Englander SW, Downer NW, & Teitelbaum H (1972). Hydrogen exchange. Annual Review of Biochemistry, 41, 903–924.

Ernst RR, Bodenhausen G, & Wokaun A (1987). Heteronuclear polarization transfer In Principles of nuclear magnetic resonance in one and two dimensions. New York: Oxford University Press.

Esadze A, Chen C, Zandarashvili L, Roy S, Pettitt BM, & Iwahara J (2016). Changes in conformational dynamics of basic side chains upon protein-DNA association. Nucleic Acids Research, 44(14), 6961–6970. [PubMed: 27288446]

Esadze A, Li DW, Wang T, Brüschweiler R, & Iwahara J (2011). Dynamics of lysine side-chain amino groups in a protein studied by heteronuclear ^{1}H-^{15}N NMR spectroscopy. Journal of the American Chemical Society, 133, 909–919. [PubMed: 21186799]

Esadze A, Zandarashvili L, & Iwahara J (2014). Effective strategy to assign ^{1}H-^{15}N heteronuclear correlation NMR signals from lysine side-chain NH_3^+ groups of proteins at low temperature. Journal of Biomolecular NMR, 60(1), 23–27. [PubMed: 25129623]

Fennell CJ, Bizjak A, Vlachy V, & Dill KA (2009). Ion pairing in molecular simulations of aqueous alkali halide solutions. The Journal of Physical Chemistry. B, 113(19), 6782–6791. [PubMed: 19206510]

Fitch CA, Platzer G, Okon M, Garcia-Moreno BE, & McIntosh LP (2015). Arginine: Its pKa value revisited. Protein Science, 24(5), 752–761. [PubMed: 25808204]

Frederick KK, Sharp KA, Warischalk N, & Wand AJ (2008). Re-evaluation of the model-free analysis of fast internal motion in proteins using NMR relaxation. The Journal of Physical Chemistry. B, 112(38), 12095–12103. [PubMed: 18759409]

Frederiksen JK, & Piccirilli JA (2009). Separation of RNA phosphorothioate oligonucleotides by HPLC. Methods in Enzymology, 468, 289–309. [PubMed: 20946775]

Gerecht K, Figueiredo AM, & Hansen DF (2017). Determining rotational dynamics of the guanidino group of arginine side chains in proteins by carbon-detected NMR. Chemical Communications (Cambridge), 53(72), 10062–10065.

Grzesiek S, & Bax A (1993). The importance of not saturating H_2O in protein NMR. Application to sensitivity enhancement and NOE measurements. Journal of the American Chemical Society, 115, 12593–12594.

Grzesiek S, Cordier F, Jaravine V, & Barfield M (2004). Insights into biomolecular hydrogen bonds from hydrogen bond scalar couplings. Progress in NMR Spectroscopy, 45(3–4), 275–300.

Gu Y, Li DW, & Brüschweiler R (2014). NMR order parameter determination from long molecular dynamics trajectories for objective comparison with experiment. Journal of Chemical Theory and Computation, 10(6), 2599–2607. [PubMed: 26580780]

Hansen DF, & Kay LE (2007). Improved magnetization alignment schemes for spin-lock relaxation experiments. Journal of Biomolecular NMR, 37(4), 245–255. [PubMed: 17310328]

Hansen DF, Vallurupalli P, & Kay LE (2008). An improved ^{15}N relaxation dispersion experiment for the measurement of millisecond time-scale dynamics in proteins. The Journal of Physical Chemistry. B, 112(19), 5898–5904. [PubMed: 18001083]

Harbison GS (1993). Interference between J-couplings and cross-relaxation in solution NMR-spectroscopy—Consequences for macromolecular structure determination. Journal of the American Chemical Society, 115(7), 3026–3027.

Hass MA, & Mulder FA (2015). Contemporary NMR studies of protein electrostatics. Annual Review of Biophysics, 44, 53–75.

Honig B, & Nicholls A (1995). Classical electrostatics in biology and chemistry. Science, 268(5214), 1144–1149. [PubMed: 7761829]

Hu JS, & Bax A (1997). χ_1 angle information from a simple two-dimensional NMR experiment that identifies trans $^3J_{NC\gamma}$ couplings in isotopically enriched proteins. Journal of Biomolecular NMR, 9(3), 323–328. [PubMed: 9204558]

Huang J, & MacKerell AD Jr. (2013). CHARMM36 all-atom additive protein force field: Validation based on comparison to NMR data. Journal of Computational Chemistry, 34(25), 2135–2145. [PubMed: 23832629]

Idiyatullin D, Daragan VA, & Mayo KH (2001). Improved measurement of ^{15}N-{^1H} NOEs in the presence of H(N)-water proton chemical exchange. Journal of Magnetic Resonance, 153(1), 138–143. [PubMed: 11700091]

Iwahara J, & Clore GM (2006). Sensitivity improvement for correlations involving arginine side-chain Nε/Hε resonances in multi-dimensional NMR experiments using broadband ^{15}N 180° pulses. Journal of Biomolecular NMR, 36(4), 251–257. [PubMed: 17036160]

Iwahara J, Esadze A, & Zandarashvili L (2015). Physicochemical properties of ion pairs of biological macromolecules. Biomolecules, 5(4), 2435–2463. [PubMed: 26437440]

Iwahara J,Jung YS, & Clore GM (2007). Heteronuclear NMR spectroscopy for lysine NH_3 groups in proteins: Unique effect of water exchange on ^{15}N transverse relaxation. Journal of the American Chemical Society, 129(10), 2971–2980. [PubMed: 17300195]

Iwahara J, Peterson RD, & Clubb RT (2005). Compensating increases in protein backbone flexibility occur when the Dead ringer AT-rich interaction domain (ARID) binds DNA: A nitrogen-15 relaxation study. Protein Science, 14(5), 1140–1150. [PubMed: 15802641]

Iwahara J, Zandarashvili L, Kemme CA, & Esadze A (2018). NMR-based investigations into target DNA search processes of proteins. Methods. 10.1016/j.ymeth.2018.05.004.

Jaravine VA, Alexandrescu AT, & Grzesiek S (2001). Observation of the closing of individual hydrogen bonds during TFE-induced helix formation in a peptide. Protein Science, 10(5), 943–950. [PubMed: 11316874]

Karplus M (1959). Contact electron-spin coupling of nuclear magnetic moments. The Journal of Chemical Physics, 30(1), 11–15.

Karplus M, & Kushick JN (1981). Method for estimating the configurational entropy of macromolecules. Macromolecules, 14(2), 325–332.

Kasinath V, Sharp KA, & Wand AJ (2013). Microscopic insights into the NMR relaxation-based protein conformational entropy meter. Journal of the American Chemical Society, 135(40), 15092–15100. [PubMed: 24007504]

Kay LE, Bull TE, Nicholson LK, Griesinger C, Schwalbe H, Bax A, et al. (1992). The measurement of heteronuclear transverse relaxation-times in AX_3 spin systems via polarization-transfer techniques. Journal of Magnetic Resonance, 100(3), 538–558.

Kay LE, & Torchia DA (1991). The effects of dipolar cross-correlation on ^{13}C methylcarbon T_1, T_2, and NOE measurements in macromolecules. Journal of Magnetic Resonance, 95(3), 536–547.

Korzhnev DM, Tischenko EV, & Arseniev AS (2000). Off-resonance effects in ^{15}N T_2 CPMG measurements. Journal of Biomolecular NMR, 17(3), 231–237. [PubMed: 10959630]

Kougentakis CM, Grasso EM, Robinson AC, Caro JA, Schlessman JL, Majumdar A, et al. (2018). Anomalous properties of Lys residues buried in the hydrophobic interior of a protein revealed with ^{15}N-detect NMR spectroscopy. Journal of Physical Chemistry Letters, 9(2), 383–387.

Kuboniwa H, Grzesiek S, Delaglio F, & Bax A (1994). Measurement of H-N-H-alpha J-couplings in calcium-free calmodulin using new 2D and 3D water-flip-back methods. Journal of Biomolecular NMR, 4(6), 871–878. [PubMed: 7812158]

Kumar A, Grace RCR, & Madhu PK (2000). Cross-correlations in NMR. Progress in NMR Spectroscopy, 37(3), 191–319.

Kupče E, Boyd J, & Campbell ID (1995). Short selective pulses for biochemical applications. Journal of Magnetic Resonance. Series B, 106(3), 300–303. [PubMed: 7719630]

Levy RM, Sheridan RP, Keepers JW, Dubey GS, Swaminathan S, & Karplus M (1985). Molecular dynamics of myoglobin at 298 K. Results from a 300-ps computer simulation. Biophysical Journal, 48(3), 509–518. [PubMed: 3840041]

Li DW, & Brüschweiler R (2009). A dictionary for protein side-chain entropies from NMR order parameters. Journal of the American Chemical Society, 131(21), 7226–7227. [PubMed: 19422234]

Li YC, & Montelione GT (1994). Overcoming solvent saturation-transfer artifacts in protein NMR at neutral pH—Application of pulsed-field gradients in measurements of ^{15}N Overhauser effects. Journal of Magnetic Resonance. Series B, 105(1), 45–51. [PubMed: 7921670]

Liepinsh E, & Otting G (1996). Proton exchange rates from amino acid side chains—Implications for image contrast. Magnetic Resonance in Medicine, 35(1), 30–42. [PubMed: 8771020]

Lipari G, & Szabo A (1982). Model-free approach to the interpretation of nuclear magnetic-resonance relaxation in macromolecules. 1. Theory and range of validity. Journal of the American Chemical Society, 104(17), 4546–4559.

Lipari G, Szabo A, & Levy RM (1982). Protein dynamics and NMR relaxation—Comparison of simulations with experiment. Nature, 300(5888), 197–198.

Löhr F, & Rüterjans H (1998). Detection of nitrogen-nitrogen J-couplings in proteins. Journal of Magnetic Resonance, 132(1), 130–137.

Loria JP, Berlow RB, & Watt ED (2008). Characterization of enzyme motions by solution NMR relaxation dispersion. Accounts of Chemical Research, 41(2), 214–221. [PubMed: 18281945]

Luscombe NM, Laskowski RA, & Thornton JM (2001). Amino acid-base interactions: A three-dimensional analysis of protein-DNA interactions at an atomic level. Nucleic Acids Research, 29(13), 2860–2874. [PubMed: 11433033]

Mandel AM, Akke M, & Palmer AG 3rd. (1995). Backbone dynamics of Escherichia coli ribonuclease HI: Correlations with structure and function in an active enzyme. Journal of Molecular Biology, 246(1), 144–163. [PubMed: 7531772]

Marcus Y, & Hefter G (2006). Ion pairing. Chemical Reviews, 106(11), 4585–4621. [PubMed: 17091929]

Markwick PR, Sprangers R, & Sattler M (2003). Dynamic effects on J-couplings across hydrogen bonds in proteins. Journal of the American Chemical Society, 125(3), 644–645. [PubMed: 12526659]

Masnovi JM, & Kochi JK (1985). Direct observation of ion-pair dynamics. Journal of the American Chemical Society, 107(26), 7880–7893.

Masunov A, & Lazaridis T (2003). Potentials of mean force between ionizable amino acid side chains in water. Journal of the American Chemical Society, 125(7), 1722–1730. [PubMed: 12580597]

Meiboom S, & Gill D (1958). Modified spin-echo method for measuring nuclear relaxation times. The Review of Scientific Instruments, 29, 688–691.

Mittermaier AK, & Kay LE (2009). Observing biological dynamics at atomic resolution using NMR. Trends in Biochemical Sciences, 34(12), 601–611. [PubMed: 19846313]

Nguyen D, Hoffpauir ZA, & Iwahara J (2017). Internal motions of basic side chains of the Antennapedia homeodomain in the free and DNA-bound states. Biochemistry, 56(44), 5866–5869. [PubMed: 29045141]

Nguyen D, & Iwahara J (2018). Impact of ^{15}N-^{15}N scalar couplings on ^{15}N transverse relaxation measurements for arginine side chains of proteins. Journal of Biomolecular NMR, 71(1), 45–51. [PubMed: 29845493]

Nguyen D, Lokesh GLR, Volk DE, & Iwahara J (2017). A unique and simple approach to improve sensitivity in ^{15}N-NMR relaxation measurements for NH_3^+ groups: Application to a protein-DNA complex. Molecules, 22(8), 1355.

Nguyen D, Zandarashvili L, White MA, & Iwahara J (2016). Stereospecific effects of oxygen-to-sulfur substitution in DNA phosphate on ion pair dynamics and protein-DNA affinity. Chembiochem, 17(17), 1636–1642. [PubMed: 27271797]

Nicholson LK, Kay LE, Baldisseri DM, Arango J, Young PE, Bax A, et al. (1992). Dynamics of methyl groups in proteins as studied by proton-detected ^{13}C NMR spectroscopy. Application to the leucine residues of staphylococcal nuclease. Biochemistry, 31(23), 5253–5263. [PubMed: 1606149]

Nieto PM, Birdsall B, Morgan WD, Frenkiel TA, Gargaro AR, & Feeney J (1997). Correlated bond rotations in interactions of arginine residues with ligand carboxylate groups in protein ligand complexes. FEBS Letters, 405(1), 16–20. [PubMed: 9094416]

O'Brien ES, Wand AJ, & Sharp KA (2016). On the ability of molecular dynamics force fields to recapitulate NMR derived protein side chain order parameters. Protein Science, 25(6), 1156–1160. [PubMed: 26990788]

Ollerenshaw JE, Tugarinov V, & Kay LE (2003). Methyl TROSY: Explanation and experimental verification. Magnetic Resonance in Chemistry, 41(10), 843–852.

Palmer AG 3rd. (2014). Chemical exchange in biomacromolecules: Past, present, and future. Journal of Magnetic Resonance, 241, 3–17. [PubMed: 24656076]

Palmer AG, Rance M, & Wright PE (1991). Intramolecular motions of a zinc finger DNA-binding domain from Xfin characterized by proton-detected natural abundance ^{13}C heteronuclear NMR-spectroscopy. Journal of the American Chemical Society, 113(12), 4371–4380.

Palmer AG, Wright PE, & Rance M (1991). Measurement of relaxation-time constants for methyl-groups by proton-detected heteronuclear NMR-spectroscopy. Chemical Physics Letters, 185(1–2), 41–46.

Perez C, Löhr F, Rüterjans H, & Schmidt JM (2001). Self-consistent Karplus parametrization of 3J couplings depending on the polypeptide side-chain torsion χ_1. Journal of the American Chemical Society, 123(29), 7081–7093. [PubMed: 11459487]

Peters KS, & Li BL (1994). Picosecond dynamics of contact ion-pairs and solvent-separated ion-pairs in the photosolvolysis of diphenylmethyl chloride. The Journal of Physical Chemistry, 98(2), 401–403.

Pettitt BM, & Rossky PJ (1986). Alkali-halides in water—Ion solvent correlations and ion ion potentials of mean force at infinite dilution. The Journal of Chemical Physics, 84(10), 5836–5844.

Platzer G, Okon M, & McIntosh LP (2014). pH-dependent random coil ^{1}H, ^{13}C, and ^{15}N chemical shifts of the ionizable amino acids: A guide for protein pK_a measurements. Journal of Biomolecular NMR, 60(2–3), 109–129. [PubMed: 25239571]

Poon DK, Schubert M, Au J, Okon M, Withers SG, & McIntosh LP (2006). Unambiguous determination of the ionization state of a glycoside hydrolase active site lysine by ^{1}H-^{15}N heteronuclear correlation spectroscopy. Journal of the American Chemical Society, 128(48), 15388–15389. [PubMed: 17132001]

Privalov PL, Dragan AI, & Crane-Robinson C (2011). Interpreting protein/DNA interactions: Distinguishing specific from non-specific and electrostatic from non-electrostatic components. Nucleic Acids Research, 39(7), 2483–2491. [PubMed: 21071403]

Renner C, Schleicher M, Moroder L, & Holak TA (2002). Practical aspects of the 2D ^{15}N-{^{1}H}-NOE experiment. Journal of Biomolecular NMR, 23(1), 23–33. [PubMed: 12061715]

Rohs R, Jin X, West SM,Joshi R, Honig B, & Mann RS (2010). Origins of specificity in protein-DNA recognition. Annual Review of Biochemistry, 79, 233–269.

Sarkar SK, Hiyama Y, Niu CH, Young PE, Gerig JT, & Torchia DA (1987). Molecular dynamics of collagen side chains in hard and soft tissues. A multinuclear magnetic resonance study. Biochemistry, 26(21), 6793–6800. [PubMed: 3427044]

Segawa T, Kateb F, Duma L, Bodenhausen G, & Pelupessy P (2008). Exchange rate constants of invisible protons in proteins determined by NMR spectroscopy. Chembiochem, 9(4), 537–542. [PubMed: 18247446]

Sepuru KM, Iwahara J, & Rajarathnam K (2018). Direct detection of lysine side chain NH_3^+ in protein-heparin complexes using NMR spectroscopy. Analyst, 143(3), 635–638. [PubMed: 29292440]

Sheinerman FB, Norel R, & Honig B (2000). Electrostatic aspects of protein-protein interactions. Current Opinion in Structural Biology, 10(2), 153–159. [PubMed: 10753808]

Skelton NJ, Palmer AG, Akke M, Kordel J, Rance M, & Chazin WJ (1993). Practical aspects of 2-dimensional proton-detected ^{15}N spin relaxation measurements. Journal of Magnetic Resonance. Series B, 102(3), 253–264.

Spyracopoulos L (2006). A suite of Mathematica notebooks for the analysis of protein main chain ^{15}N NMR relaxation data. Journal of Biomolecular NMR, 36(4), 215–224. [PubMed: 17061025]

Szwarc M (1972). Ions and ion pairs in organic reactions. Vol. 1 New York: Wiley-Interscience.

Takayama Y, Castaneda CA, Chimenti M, Garcia-Moreno B, & Iwahara J (2008). Direct evidence for deprotonation of a lysine side chain buried in the hydrophobic core of a protein. Journal of the American Chemical Society, 130(21), 6714–6715. [PubMed: 18454523]

Takeda M, Hallenga K, Shigezane M, Waelchli M, Lohr F, Markley JL, et al. (2011). Construction and performance of an NMR tube with a sample cavity formed within magnetic susceptibility-matched glass. Journal of Magnetic Resonance, 209(2), 167–173. [PubMed: 21316281]

Tjandra N, Feller SE, Pastor RW, & Bax A (1995). Rotational diffusion anisotropy of human ubiquitin from ^{15}N NMR relaxation. Journal of the American Chemical Society, 117(50), 12562–12566.

Tjandra N, Szabo A, & Bax A (1996). Protein backbone dynamics and ^{15}N chemical shift anisotropy from quantitative measurement of relaxation interference effects. Journal of the American Chemical Society, 118(29), 6986–6991.

Tomlinson JH, Ullah S, Hansen PE, & Williamson MP (2009). Characterization of salt bridges to lysines in the protein G B1 domain. Journal of the American Chemical Society, 131(13), 4674–4684. [PubMed: 19281232]

Trbovic N, Cho JH, Abel R, Friesner RA, Rance M, & Palmer AG 3rd., (2009). Protein side-chain dynamics and residual conformational entropy. Journal of the American Chemical Society, 131(2), 615–622. [PubMed: 19105660]

van de Ven FJM (1995). Dephasing coherences In Multidimensional NMR in liquids: Basic principles and experimental methods (pp. 211–224). New York: VCH Publishers.

van Zijl PCM, Sukumar S, Johnson MO, Webb P, & Hurd RE (1994). Optimized shimming for high-resolution NMR using 3-dimensional image-based field mapping. Journal of Magnetic Resonance. Series A, 111(2), 203–207.

Voehler MW, Collier G, Young JK, Stone MP, & Germann MW (2006). Performance of cryogenic probes as a function of ionic strength and sample tube geometry. Journal of Magnetic Resonance, 183(1), 102–109. [PubMed: 16949320]

Wand AJ (2013). The dark energy of proteins comes to light: Conformational entropy and its role in protein function revealed by NMR relaxation. Current Opinion in Structural Biology, 23(1), 75–81. [PubMed: 23246280]

Wand AJ, & Sharp KA (2018). Measuring entropy in molecular recognition by proteins. Annual Review of Biophysics.

Werbeck ND, Kirkpatrick J, & Hansen DF (2013). Probing arginine side-chains and their dynamics with carbon-detected NMR spectroscopy: Application to the 42 kDa human histone deacetylase 8

at high pH. Angewandte Chemie (International Ed. in English), 52(11), 3145–3147. [PubMed: 23401322]

Woessner DE (1962). Nuclear spin relaxation in ellipsoids undergoing rotational Brownian motion. The Journal of Chemical Physics, 37, 647–654.

Yamazaki T, Pascal SM, Singer AU, Formankay JD,& Kay LE (1995). Nmr pulse schemes for the sequence-specific assignment of arginine guanidino ^{15}N and ^{1}H chemical-shifts in proteins. Journal of the American Chemical Society, 117(12), 3556–3564.

Yao L, Grishaev A, Cornilescu G, & Bax A (2010). Site-specific backbone amide ^{15}N chemical shift anisotropy tensors in a small protein from liquid crystal and cross-correlated relaxation measurements. Journal of the American Chemical Society, 132(12), 4295–4309. [PubMed: 20199098]

Yuwen T, & Skrynnikov NR (2014a). CP-HISQC: A better version of HSQC experiment for intrinsically disordered proteins under physiological conditions. Journal of Biomolecular NMR, 58(3), 175–192. [PubMed: 24496557]

Yuwen T, & Skrynnikov NR (2014b). Proton-decoupled CPMG: A better experiment for measuring ^{15}N R_2 relaxation in disordered proteins. Journal of Magnetic Resonance, 241, 155–169. [PubMed: 24120537]

Zandarashvili L, Esadze A, & Iwahara J (2013). NMR studies on the dynamics of hydrogen bonds and ion pairs involving lysine side chains of proteins. Advances in Protein Chemistry and Structural Biology, 93, 37–80. [PubMed: 24018322]

Zandarashvili L, Esadze A, Kemme CA, Chattopadhyay A, Nguyen D, & Iwahara J (2016). Residence times of molecular complexes in solution from NMR data of intermolecular hydrogen-bond scalar coupling. Journal of Physical Chemistry Letters, 7(5), 820–824.

Zandarashvili L, Esadze A, Vuzman D, Kemme CA, Levy Y, & Iwahara J (2015). Balancing between affinity and speed in target DNA search by zinc-finger proteins via modulation of dynamic conformational ensemble. Proceedings of the National Academy of Sciences of the United States of America, 112(37), E5142–E5149. [PubMed: 26324943]

Zandarashvili L, & Iwahara J (2015). Temperature dependence of internal motions of protein side-chain NH_3^+ groups: Insight into energy barriers for transient breakage of hydrogen bonds. Biochemistry, 54(2), 538–545. [PubMed: 25489884]

Zandarashvili L, Li DW, Wang T, Brüschweiler R, & Iwahara J (2011). Signature of mobile hydrogen bonding of lysine side chains from long-range ^{15}N-^{13}C scalar J-couplings and computation. Journal of the American Chemical Society, 133(24), 9192–9195. [PubMed: 21591797]

Zandarashvili L, Nguyen D, Anderson KM, White MA, Gorenstein DG, & Iwahara J (2015). Entropic enhancement of protein-DNA affinity by oxygen-to-sulfur substitution in DNA phosphate. Biophysical Journal, 109(5), 1026–1037. [PubMed: 26331260]

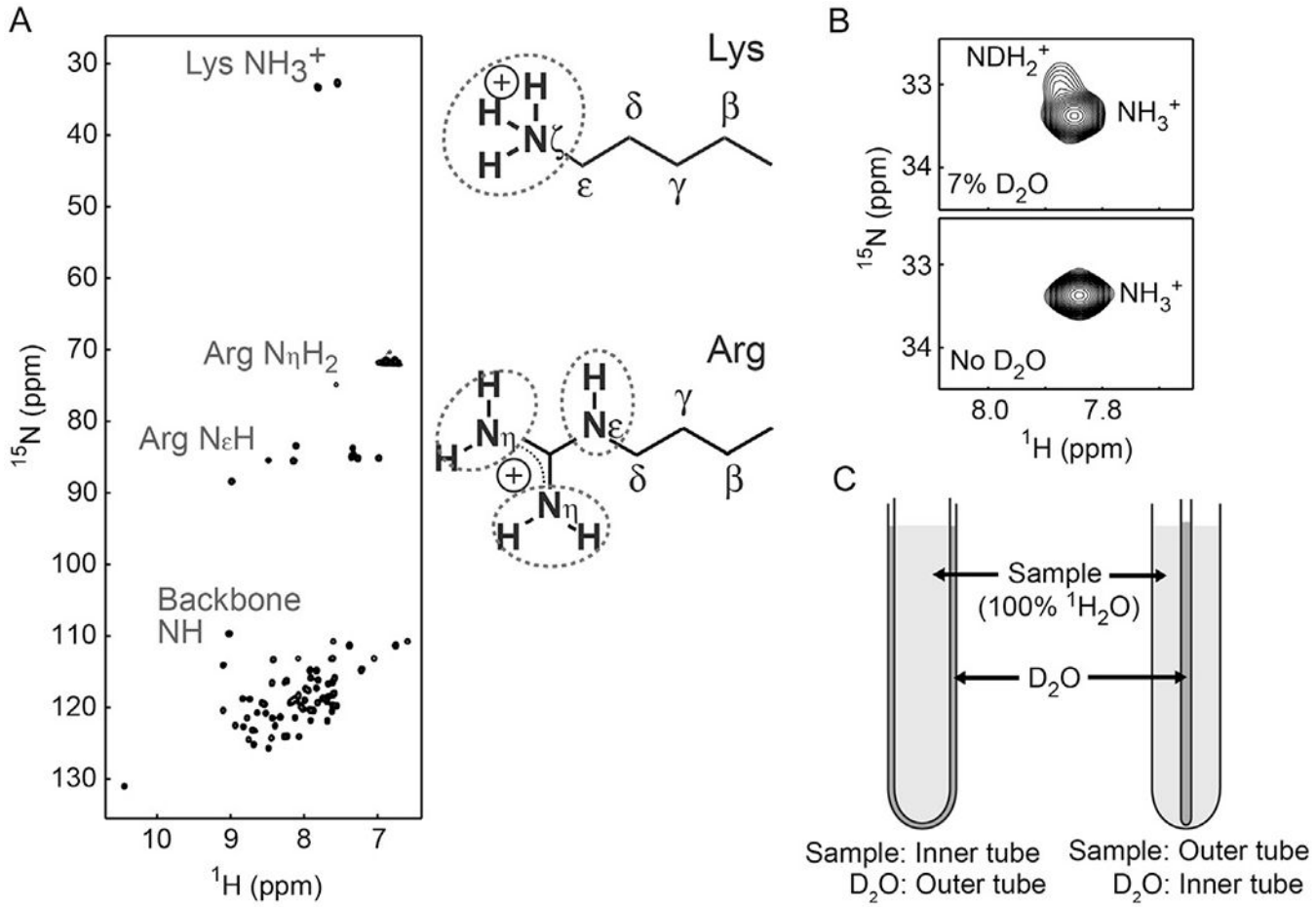

Fig. 1.

(A) ^{1}H and ^{15}N resonances of the Lys and Arg side chains of the HoxD9 homeodomain bound to 24-bp specific DNA at 35°C. (B) Effect of D_2O in the sample buffer. D_2O for NMR lock should separately be sealed to avoid exchange between isotopically different species (i.e., NH_3^+, NDH_2^+, ND_2H^+). (C) Two types of coaxial NMR tubes for separating the sample and D_2O.

A

Terms	Scalar relaxation rates
$8N_yH_zH_zH_z$	$3(\rho_{HH}+k_{ex,w})$
$4N_yH_zH_z$	$2(\rho_{HH}+k_{ex,w})$
$2N_yH_z$	$\rho_{HH}+k_{ex,w}$
N_y	0

B

^{15}N line broadening (in Hz) due to hydrogen exchange		
	Lys NH_3^+	Arg $N_\varepsilon H$
HMQC	$2k_{ex,w}/\pi$	$k_{ex,w}/\pi$
HSQC	$1.5k_{ex,w}/\pi$	$0.5k_{ex,w}/\pi$
HISQC	0	0

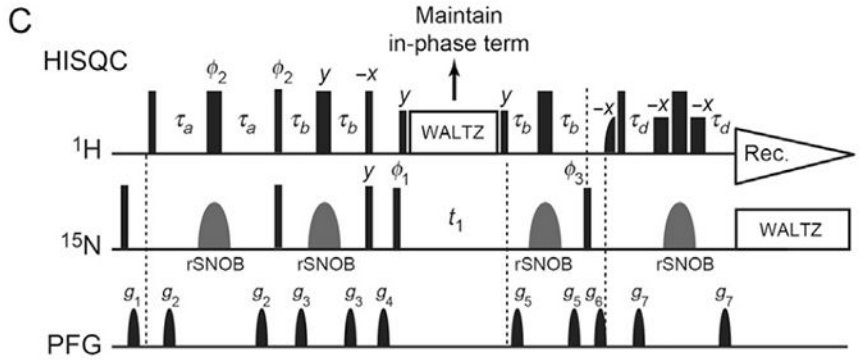

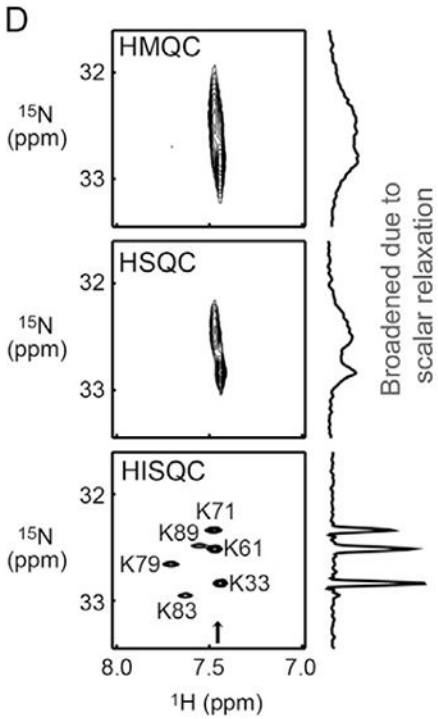

Fig. 2.

The importance of maintaining the in-phase single-quantum term during the ^{15}N evolution period in ^{1}H–^{15}N NMR experiments for Lys and Arg side chains. (A) Impact of scalar relaxation on different single-quantum terms of ^{15}N coherence. (B) Broadening of ^{15}N line shapes due to hydrogen exchange in the ^{15}N dimensions of HSQC, HMQC, and HISQC spectra for Lys NH_3^+ and Arg $N_\varepsilon H$ groups. The increases in ^{15}N half-height widths are given in Hz units. (C) The pulse sequence of the water-flip-back HISQC experiment for Lys NH_3^+ or Arg $N_\varepsilon H$ groups. *Thin* and *bold bars* in *black* represent hard rectangular 90° and 180° pulses, respectively. Water-selective half-Gaussian (2.1 ms) and soft-rectangular (1.2 ms) 90° pulses are represented by *half-bell* and *short-bold shapes*, respectively. Unless indicated otherwise, pulse phases are along x, and the carrier position for ^{1}H was set to the position of the water resonance. The ^{15}N carrier position is set to ~33 ppm for Lys NH_3^+ groups and to ~85 ppm for Arg $N_\varepsilon H$ groups. A *gray bell-shape* for ^{15}N represents a 1.0-ms rSNOB 180° pulse (Kupče, Boyd, & Campbell, 1995) selective to Lys $^{15}N_\zeta$ or Arg $^{15}N_\varepsilon$ nuclei. The delays τ_a and τ_b are set as follows: $\tau_a = 2.7$ ms and $\tau_b = 1.3$ ms for Lys NH_3^+ groups; $\tau_a = 2.3$ ms and $\tau_b = 2.7$ ms for Arg $N_\varepsilon H$ groups. This setting for Arg side chains suppresses signals from $N_\eta H_2$ groups; $\tau_b = 1.3$ ms can be used to avoid this suppression of $N_\eta H_2$ signals. Phase cycles: $\varphi_1 = (y, -y)$; $\varphi_2 = (2(y), 2(-y))$; $\varphi_3 = (4x, 4(-x))$;receiver = $(x, 2(-x), x, -x, 2x, -x)$. Quadrature detection in the t_1 domain was achieved using States-TPPI, incrementing the phase φ_1. The third ^{1}H 90° pulse along $-x$ (before the gradient g_4) serves two purposes: it purges unnecessary ^{15}N antiphase magnetization by generating multiple quantum coherence and it flips the water magnetization back to $+z$. In the HISQC experiment, ^{1}H WALTZ-16 decoupling pulses maintain ^{15}N in-phase single-quantum coherence during the ^{15}N evolution period t_1 and thereby suppress the broadening of ^{15}N line shapes due to rapid scalar relaxation arising from hydrogen exchange. (D) HISQC

drastically improves $^{1}H–^{15}N$ correlation spectra for Lys NH_3^+ groups through suppression of scalar relaxation during the ^{15}N evolution period. This panel compares the HMQC, HSQC, and HISQC spectra recorded for the Lys NH_3^+ groups of the ^{15}N-labeled Egr-1 zinc-finger–DNA complex at pH 5.8 and 10°C. For each spectrum, the data were acquired using the same number of scans and the same digital resolutions and were processed identically. F_1-slices at the position indicated by an *arrow* are shown to indicate ^{15}N line shapes.

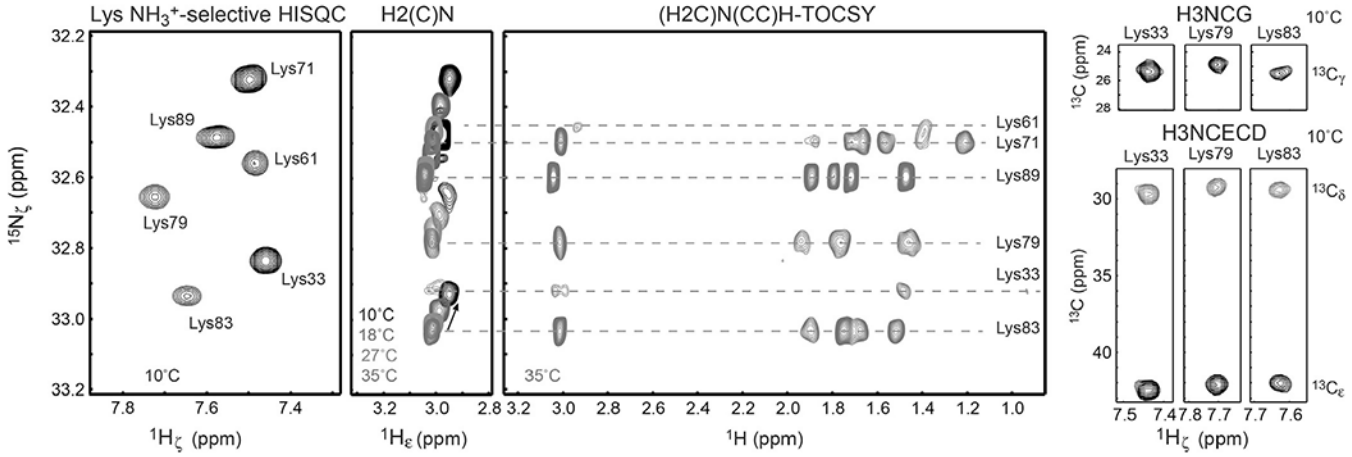

Fig. 3.

Assignment of the ^{1}H and ^{15}N resonances of Lys NH_3^+ groups using 2D ^{13}C-decoupled HISQC, 2D H2(C)N (Andre et al., 2007), 2D (H2C)N (CC)H-TOCSY (Esadze et al., 2014), 3D H3NCG (Esadze et al., 2014), and 3D H3NCECD (Esadze et al., 2014) spectra. The spectra were recorded for the $^{13}C/^{15}N$-labeled Egr-1 zinc-finger–DNA complex at indicated temperatures and pH 5.8.

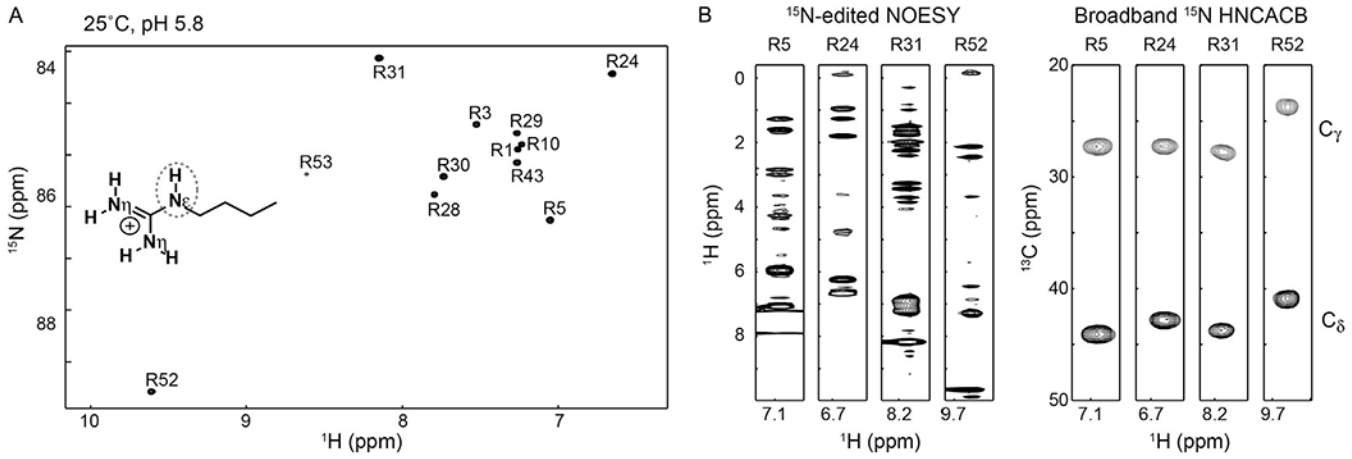

Fig. 4.

(A) ^{1}H–^{15}N HISQC spectra recorded for the Arg $N_\varepsilon H$ groups of the Antp homeodomain–DNA complex at pH 5.8 and 25°C (Nguyen, Hoffpauir, et al., 2017). (B) Strips of 3D ^{15}N-edited NOESY and broadband HNCACB (Iwahara & Clore, 2006) spectra for some Arg side chains of the Antp homeodomain–DNA complex. The broadband HNCACA spectrum shows correlation of Arg side-chain $^{1}H_\varepsilon$, $^{13}C_\gamma$, $^{13}C_\delta$, and $^{15}N_\varepsilon$ resonances.

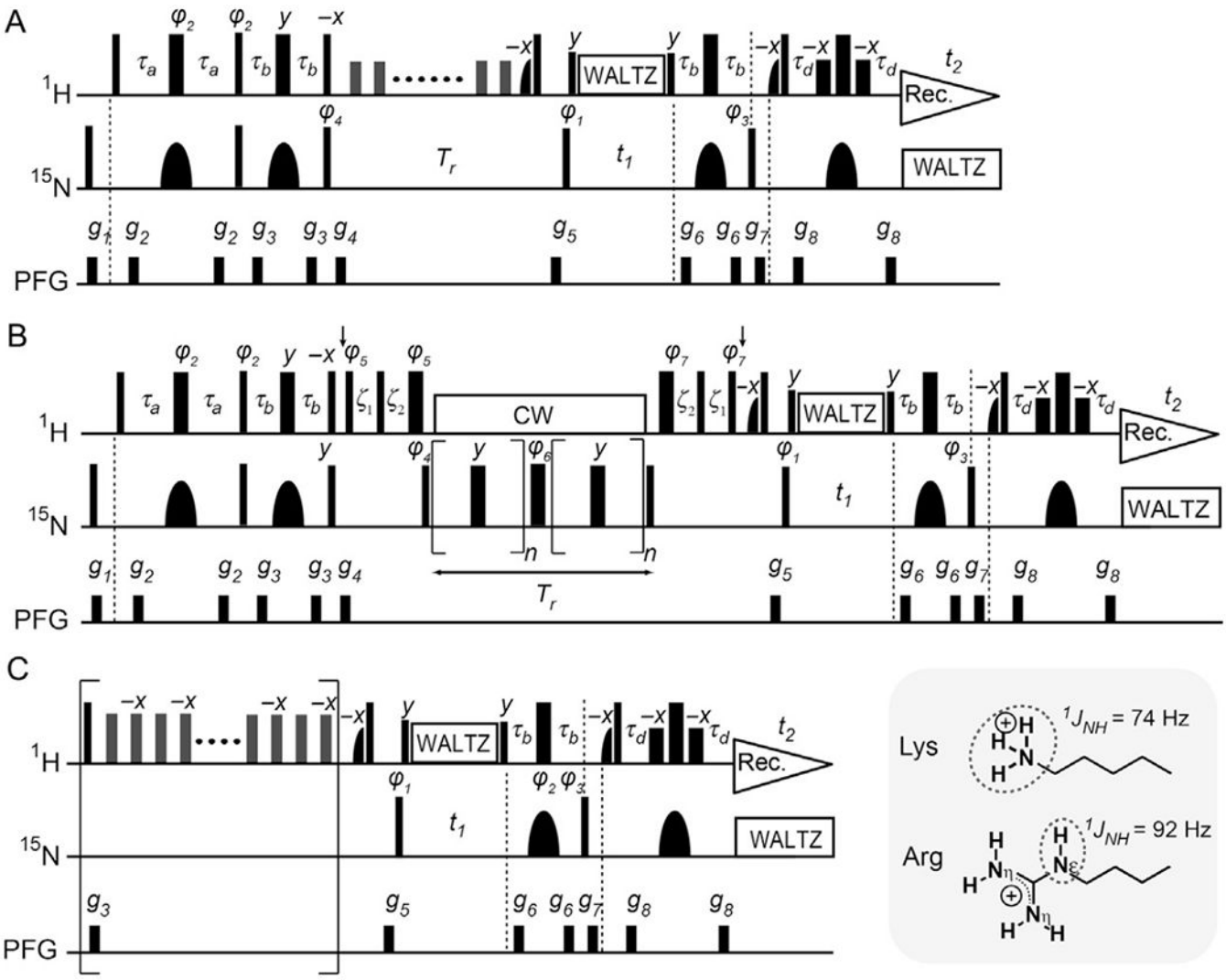

Fig. 5.

^{15}N relaxation measurements for Lys NH_3^+ and Arg $N_\varepsilon H$ groups (Esadze et al., 2016, 2011; Nguyen, Lokesh, Volk, & Iwahara, 2017). Symbols representing pulses are the same as those used in Fig. 2C. The delays τ_a = 2.7 ms and τ_b = 1.3 ms are used for Lys NH_3^+ groups, whereas τ_a = 2.3 ms and τ_b = 2.7 ms are used for Arg $N_\varepsilon H$ groups. The ^{15}N carrier position is set to ~33 pm for Lys NH_3^+ groups and to ~85 ppm for Arg $N_\varepsilon H$ groups. The ^{1}H carrier position is set to the H_2O resonance. Quadrature detection in the t_1 domain was achieved using States-TPPI, incrementing the phase φ_1. Although the use of τ_b = 1.3 ms for Lys NH_3^+ groups retains $4N_xH_zH_z$ terms, the impact of these terms is eliminated in other parts of these pulse sequences (Nguyen, Lokesh, et al., 2017). To maintain the in-phase single-quantum ^{15}N coherence, the ^{1}H WALTZ composite pulses are used during the t_1 period. (A) ^{15}N longitudinal relaxation measurement. A ^{1}H 180° pulse that does not affect H_2O resonance is applied every 10 ms during the delay T_r for longitudinal relaxation. A recycle delay between scans is set to 2 s in this experiment. Phase cycles: $\varphi_1 = (2y, 2(-y))$, $\varphi_2 = (y, -y)$, $\varphi_3 = (4x, 4(-x))$, $\varphi_4 = (8y, 8(-y))$, and receiver = $(x, -x, -x, x, 2(-x, x, x, -x), x, -x, -x, x)$. (B) ^{15}N transverse relaxation measurement. The ^{1}H carrier position is shifted to 7.8 ppm at the

position of the *first vertical arrow* (after the PFG g_4) and set back to the position of water resonance at the position of the *second arrow*. Typically we use the CPMG frequency ν_{CPMG} of 417 Hz. For this, the RF strength $\omega_{CW}/2\pi$ of ^{1}H CW during the CPMG is set to 5 kHz, satisfying $\omega_{CW}/2\pi = 2k\nu_{CPMG}$ (k, integer) (Hansen, Vallurupalli, & Kay, 2008). However, when a lower CPMG frequency is used, a stronger RF strength is required for ^{1}H CW to maintain the in-phase single-quantum ^{15}N coherence during the CPMG scheme. For Arg $N_\varepsilon H$ groups, the CPMG frequency, the RF strength, and ^{15}N carrier position should be set to avoid the recoupling conditions for modulation by $^2J_{NN}$ couplings (Nguyen & Iwahara, 2018). The delays ξ_1 and ξ_2 are for alignment of ^{1}H magnetization and given by $\xi_1 = 1/\omega_{CW} = (4/\pi)\tau_{90H}$ and $\xi_2 = \tau_{90N} - (2/\pi)\tau_{90H}$ (Hansen et al., 2008; Hansen & Kay, 2007), in which τ_{90} represents the relevant 90° pulse length. A recycle delay of 2.9 s is used. Phase cycles: $\varphi_1 = (4y, 4(-y))$, $\varphi_2 = (8y, 8(-y))$, $\varphi_3 = x, \varphi_4 = (x, -x)$, $\varphi_5 = (2y, 2(-y))$, $\varphi_6 = (2x, 2(-x))$, $\varphi_7 = (2(-y), 2y)$, and receiver = $(x, -x, x, -x, 2(-x, x, -x, x), x, -x, x, -x)$. (C) Heteronuclear ^{1}H–^{15}N NOE measurement. Measurement with ^{1}H saturation (5 s) is performed with a train of 180°x and 180°$(-x)$ pulses (RF strength, 11 kHz) at an interval of 10 ms. The reference spectrum is measured without the scheme in the *bracket*. For measurements of heteronuclear NOE, we set a recycle delay (including the saturation period) to 12s for a 600-MHz spectrometer and to 18s for 750 or 800 MHz spectrometer. Phase cycles: $\varphi_1 = (y, -y)$, $\varphi_2 = (4x, 4y, 4(-x), 4(-y))$, $\varphi_3 = (2x, 2(-x))$, and receiver = $(x, -x, -x, x, -x, x, x, -x)$.

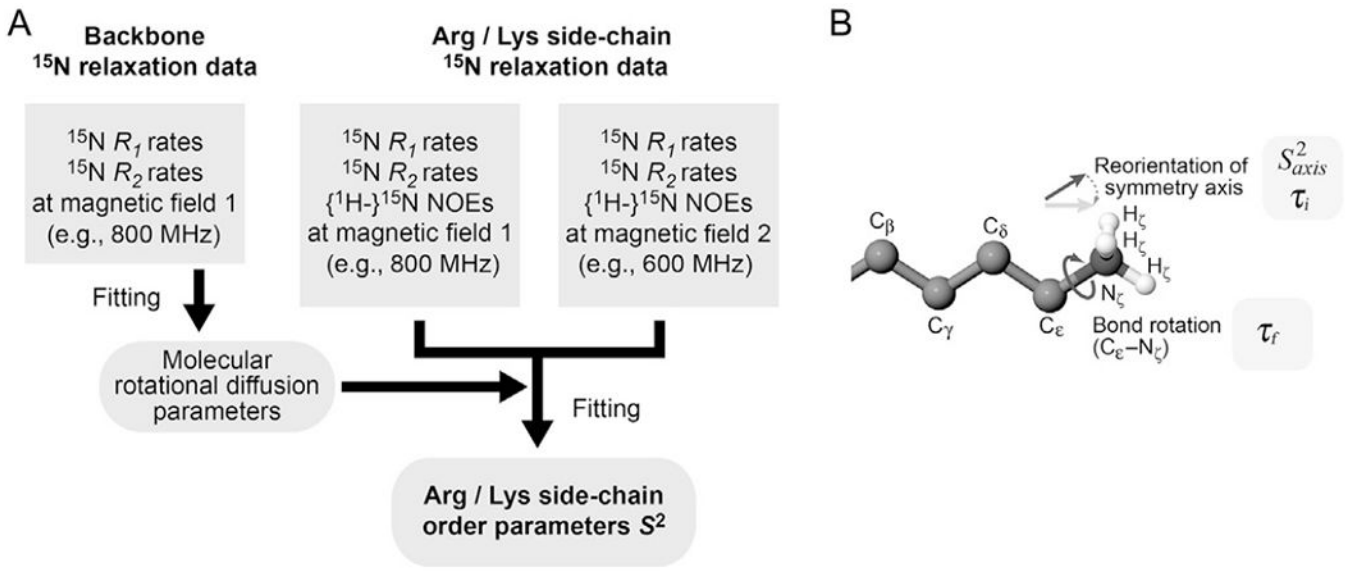

Fig. 6.

(A) Procedures for determination of the order parameters S^2 for Lys and Arg side chains. (B) Motion model for Lys side-chain NH_3^+ groups.

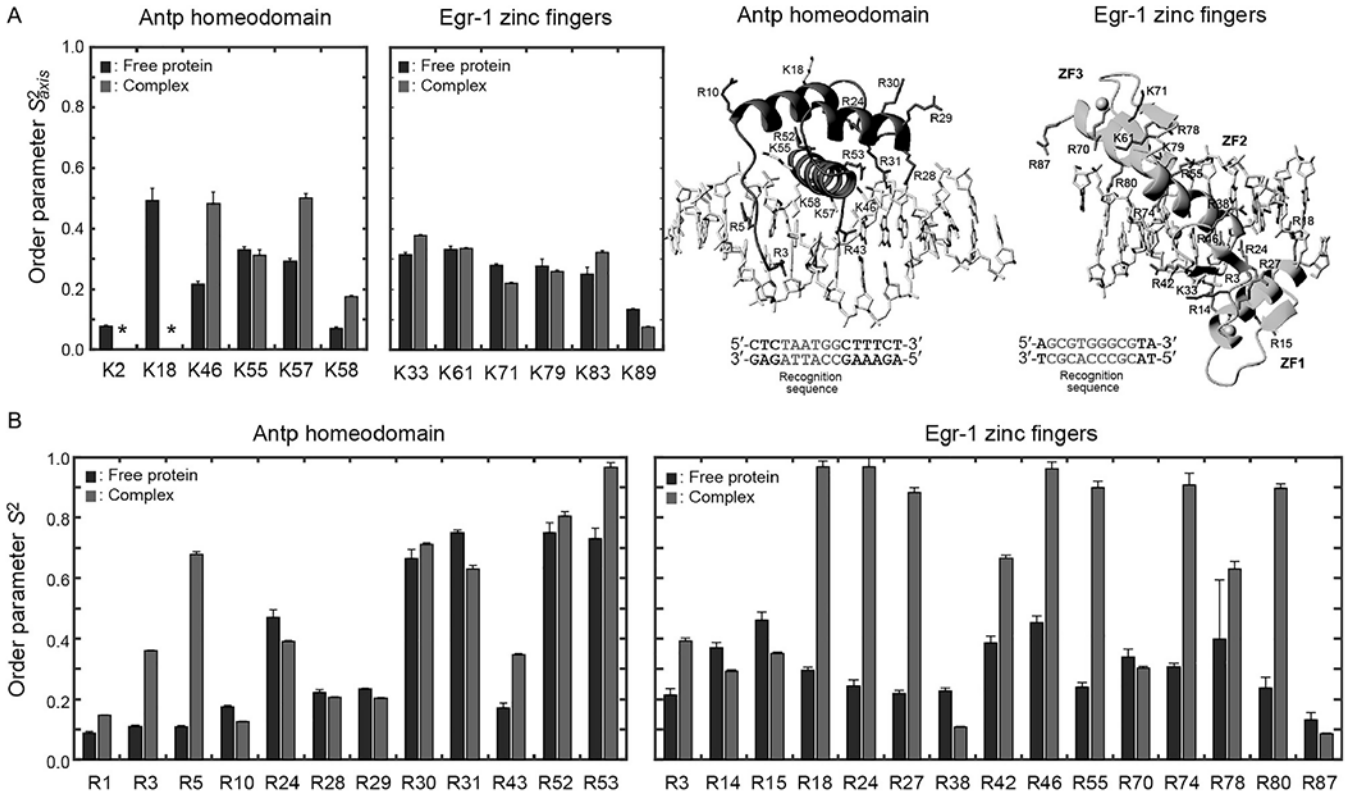

Fig. 7.

Lys and Arg side-chain order parameters determined for the Egr-1 zinc-finger protein and the Antp homeodomain in the free form and in the complexes with specific DNA (Esadze et al., 2016; Nguyen, Hoffpauir, et al., 2017).

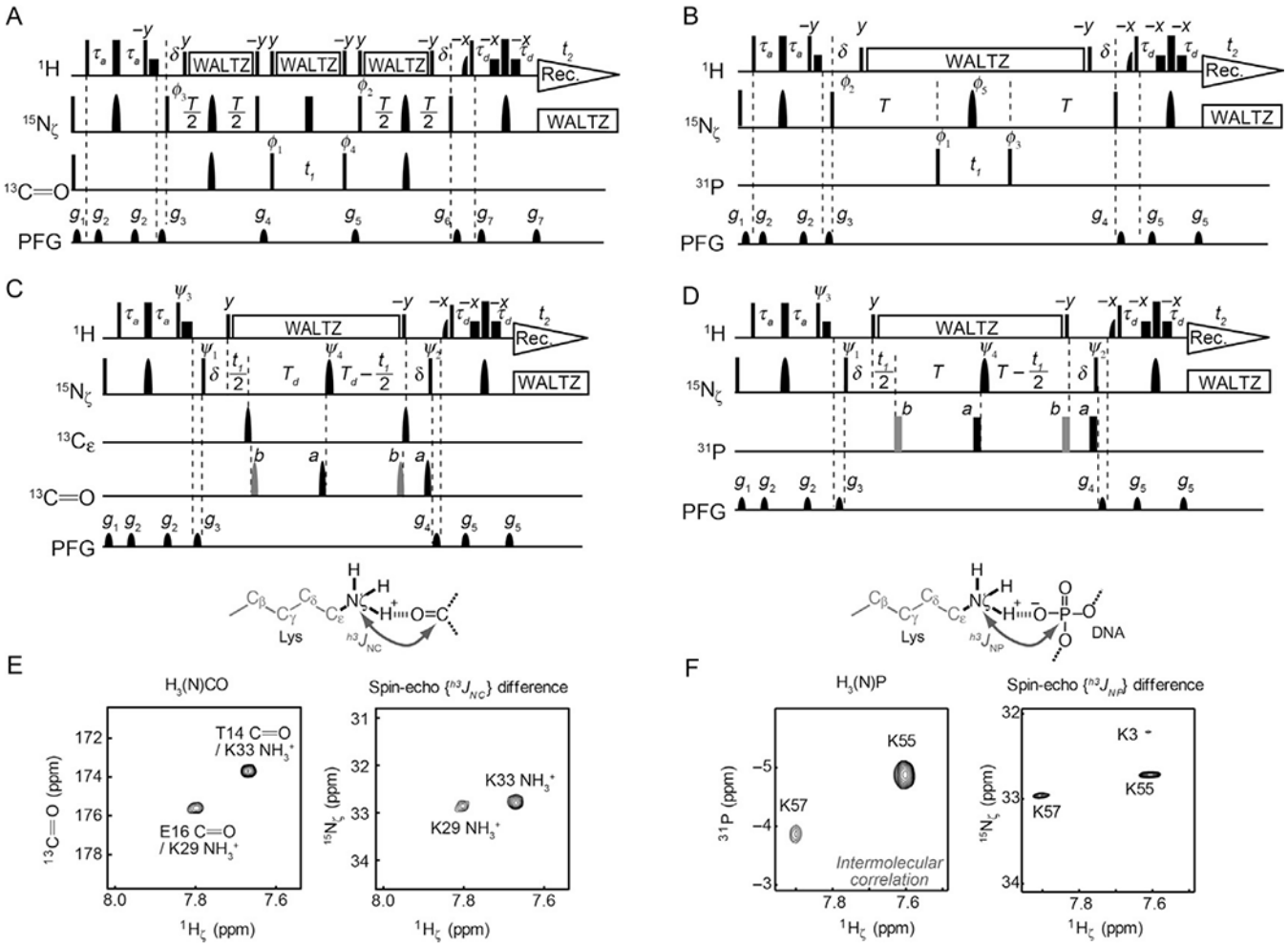

Fig. 8.

NMR experiments for observing hydrogen-bond scalar couplings of Lys NH_3^+ groups (Anderson et al., 2013; Zandarashvili et al., 2011). (A, B) 2D heteronuclear correlation experiments to observe signals arising from hydrogen-bond scalar couplings. Resonances of the coupling partner nuclei ($^{13}C{=}O$ for (A) and ^{31}P for (B)) are directly observed in these experiments. *Symbols* representing pulses are the same as those used in Fig. 2C. Shaped ^{13}C pulses represent IBURP-2 180° pulses (1.1 ms). Delays: $\tau_a = 2.7$ ms; $\delta = 2.6$ ms, $T = 212$ ms; and $T_d = 206$ ms. Carrier positions: ^1H, the position of the water resonance; ^{15}N, 33 ppm; $^{13}C_\varepsilon$, 45 ppm; $^{13}C{=}O$, 177 ppm; and ^{31}P, −3ppm (^{31}P referencing to trimethyl phosphate). Phase cycles: $\varphi_1 = (2x, 2(-x))$, $\varphi_2 = (4x, 4(-x))$, $\varphi_3 = (x, -x)$, $\varphi_4 = (8x, 8(-x))$, $\varphi_5 = (8x, 8y, 8(-x), 8(-y))$, and receiver = $(x, -x, -x, x, 2(-x, x, x, -x), x, -x, -x, x)$. Quadrature detection in the t_1 domain was achieved using States-TPPI for φ_1. (C, D) 2D spin-echo *J*-modulation constant-time HISQC experiments to measure the magnitude of $^{h3}J_{NC}$ (C) or $^{h3}J_{NP}$ (D) couplings. Phase cycles: $\psi_1 = (2x, 2(-x))$, $\psi_2 = (4x, 4(-x))$, $\psi_3 = (y, -y)$, $\psi_4 = (8x, 8y, 8(-x), 8(-y))$, and receiver = $(x, -x, -x, x, 2(-x, x, x, -x), x, -x, -x, x)$. Quadrature detection in the t_1 domain was achieved using States-TPPI for ψ_1. (E) Observation of $^{h3}J_{NC}$ couplings for the Lys NH_3^+ groups of ubiquitin (Zandarashvili et al., 2011). (F) Observation of intermolecular $^{h3}J_{NP}$ couplings between Lys side-chain ^{15}N and

DNA ^{31}P nuclei (Anderson et al., 2013). For the spin-echo *J*-modulation data, the difference spectra (i.e., subspectrum *b* minus subspectrum *a*) are shown to demonstrate the presence of the hydrogen-bond scalar couplings, although the magnitudes of these couplings are determined using the signal intensities in the individual subspectra, as described in Section 4.1.

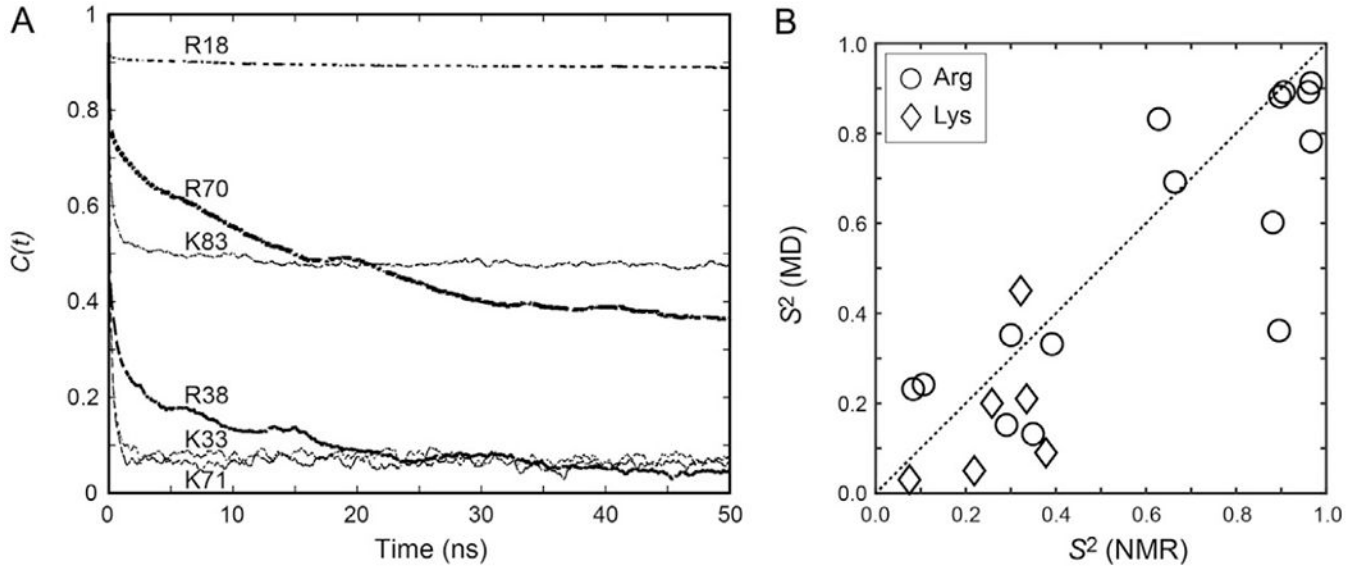

Fig. 9.

Comparison of NMR-derived vs MD-derived order parameters for the Lys and Arg side chains of the Egr-1 zinc-finger protein bound to its target DNA. (A) Examples of autocorrelation functions calculated for Lys C_ε–N_ζ and Arg $N_\varepsilon H$ bonds from 0.6-μs MD trajectories. (B) Correlation between the NMR-derived and MD-derived order parameters for the Lys NH_3^+ and Arg $N_\varepsilon H$ groups of the Egr-1–DNA complex.

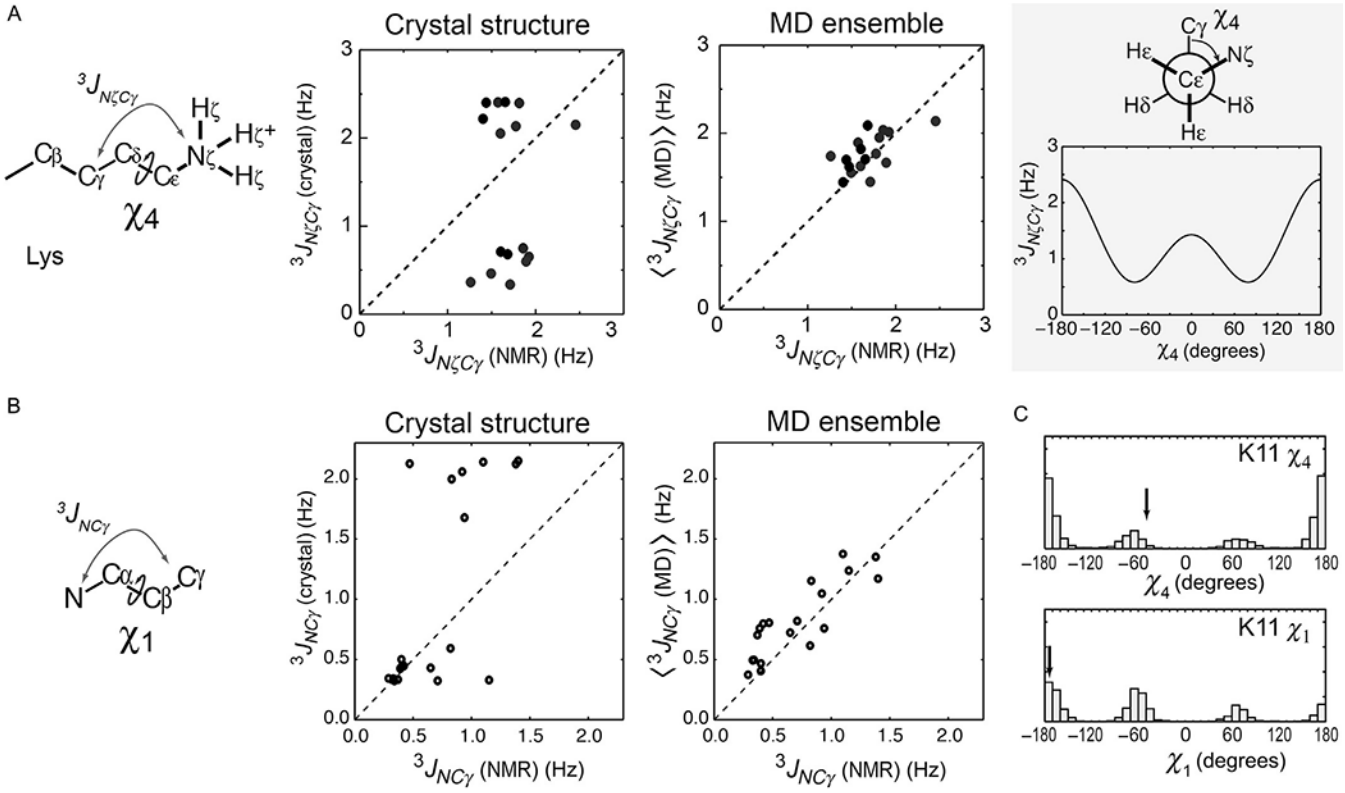

Fig. 10.

$^3J_{NC}$ coupling data indicating dynamic alterations of side-chain torsion angles. (A) Correlations between the observed and predicted χ_4-relevant $^3J_{N\zeta C\gamma}$ couplings for the Lys side chains of ubiquitin (Zandarashvili et al., 2011), the Antp homeodomain–DNA complex, and the Egr-1–DNA complex (Chen et al., 2015). The $^3J_{N\zeta C\gamma}$ couplings were predicted from crystal structures (PDB 1UBQ, 9ANT, and 1AAY) or MD ensembles. (B) Corresponding data for the $^3J_{NC\gamma}$ couplings between backbone ^{15}N and side-chain $^{13}C_\gamma$ nuclei related to the χ_1 angles of ubiquitin side chains. (C) Distribution of the χ_1 and χ_4 angles of the K11 side chain of ubiquitin in the MD trajectory (Zandarashvili et al., 2011). *Arrows* indicate the angles in the crystal structure.

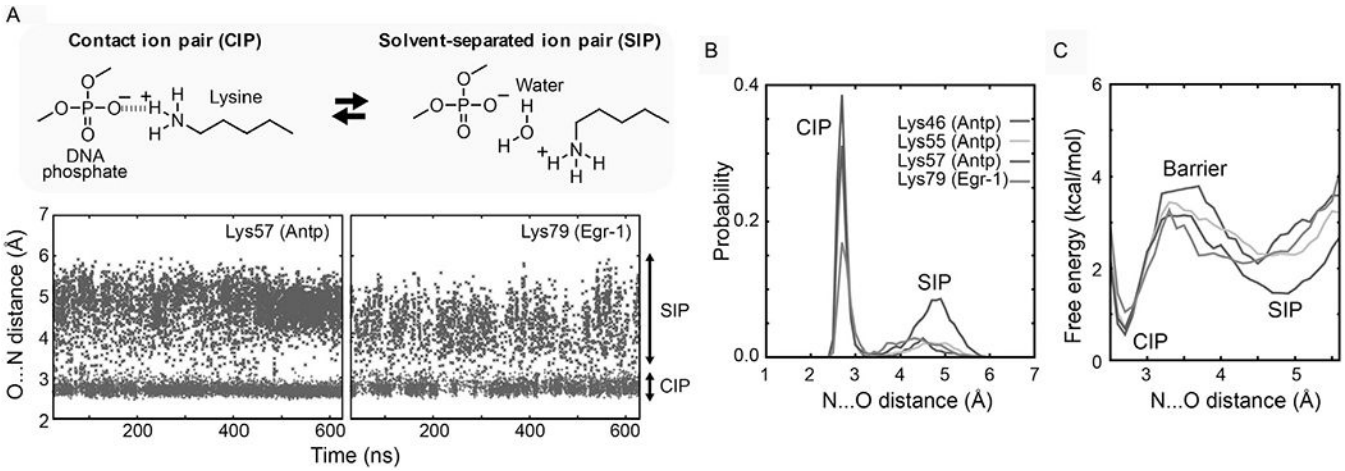

Fig. 11.

Dynamic transitions between the CIP and SIP states of the intermolecular ion pairs of Lys side-chain NH_3^+ and DNA phosphate groups observed in the 0.6-μs MD simulations for the Antp–DNA and Egr-1–DNA complexes. (A) The trajectories of the distances from the Lys N_ζ atoms to the closest DNA phosphate oxygen atoms are shown for the intermolecular ion pairs for which the presence of CIP was experimentally confirmed. (B) Probability distribution of the CIP and SIP states as a function of the distance from the Lys N_ζ atom to the closest DNA phosphate oxygen atom. (C) PMFs for the intermolecular ion pairs of the protein side-chain NH_3^+ and DNA phosphate groups in the Antp homeodomain–DNA complex and the Egr-1 zinc-finger–DNA complex.

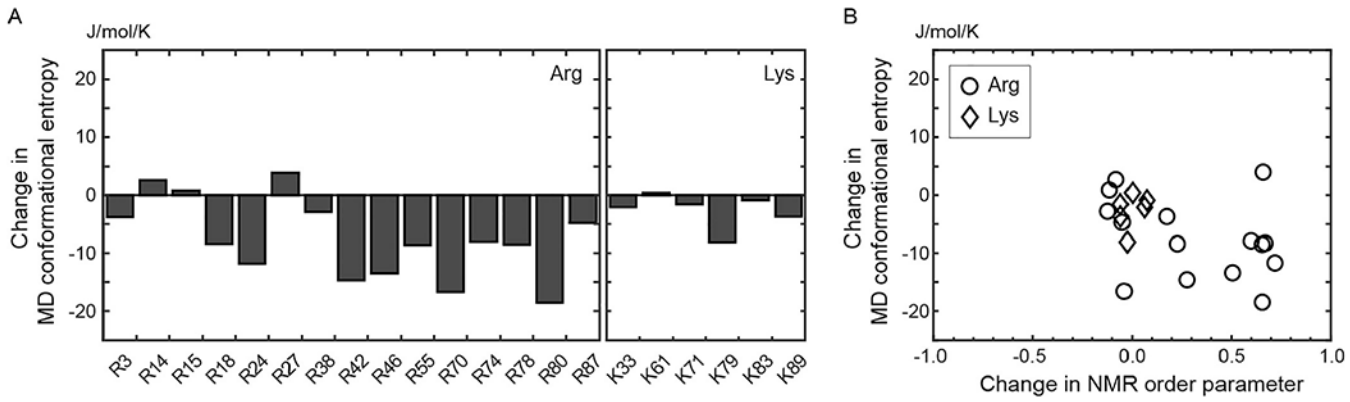

Fig. 12.

Changes in side-chain conformational entropy for the Lys and Arg side chains of the Egr-1 zinc-finger protein upon binding to the target DNA. (A) Changes in the side-chain conformational entropy of Lys and Arg side chains calculated from 0.6-μs MD trajectories for the free protein and the complex. (B) Correlation between changes in the NMR order parameters and changes in the MD conformational entropy upon complex formation.

Table 1

Typical ^{1}H, ^{13}C, and ^{15}N Chemical Shifts (in ppm) of Lys and Arg Residues[a]

	Lys		Arg	
^{1}H	H_N	7.5–8.8	H_N	7.3–9.2
	H_α	3.8–4.7	H_α	3.8–4.8
	$H_{\beta2/\beta3}$	1.5–2.0	$H_{\beta2/\beta3}$	1.4–2.1
	$H_{\gamma2/\gamma3}$	1.1–1.6	$H_{\gamma2/\gamma3}$	1.2–1.8
	$H_{\delta2/\delta3}$	1.0–2.3	$H_{\delta2/\delta3}$	2.8–3.4
	$H_{\varepsilon2/\varepsilon3}$	2.7–3.1	H_ε[b]	7.2-9.2
	$H_{\zeta1/\zeta2/\zeta3}$ (NH_3^+)[c]	7.2–8.2	$H_{\eta11/\eta12/\eta21/\eta22}$[d]	6.7–8.7
	$H_{\zeta1/\zeta2}$ (NH_2)[e]	0.8–1.2		
^{13}C	C═O	171–183	C═O	173–180
	C_α	54–60	C_α	53–60
	C_β	30–36	C_α	28–33
	C_γ	22–28	C_γ	24–30
	C_δ	26–32	C_δ	40–46
	C_ε	39–45	C_ζ	154–167
^{15}N	N (backbone)	116–126	N (backbone)	116–126
	N_ζ (NH_3^+)[c]	30–35	N_ε[b]	78–90
	N_ζ (NH_2)[f]	22–26	$N_{\eta1/\eta2}$[d]	68–74

[a] Unless indicated otherwise, data are from the Biological Magnetic Resonance Bank (BMRB). Each range corresponds to average ± standard deviation in the BMRB chemical shift statistics table.

[b] From data in the literature (e.g., Esadze et al., 2016; Nguyen, Hoffpauir, & Iwahara, 2017; Yamazaki, Pascal, Singer, Formankay, & Kay, 1995).

[c] From data in the literature (e.g., Iwahara, Jung, & Clore, 2007; Poon et al., 2006).

[d] From data in the literature (e.g., Nieto et al., 1997; Yamazaki et al., 1995).

[e] Observed only for those buried in a hydrophobic core (Kougentakis et al., 2018; Takayama, Castaneda, Chimenti, Garcia-Moreno, & Iwahara, 2008).

[f] From data in the literature (Andre et al., 2007; Kougentakis et al., 2018; Poon et al., 2006; Takayama et al., 2008).